Advances in Meteorology

Meteorological and Hydrogeological Applications: Convective Precipitation

Lead Guest Editor: Youcun Qi
Guest Editors: Ismail Gultepe, Shuai Zhang, Zhe Li, and Yong-Guang Zheng

Meteorological and Hydrogeological Applications: Convective Precipitation

Advances in Meteorology

Meteorological and Hydrogeological Applications: Convective Precipitation

Lead Guest Editor: Youcun Qi
Guest Editors: Ismail Gultepe, Shuai Zhang, Zhe Li, and Yong-Guang Zheng

Contents

Hindawi
Advances in Meteorology
Volume 2022, Article ID 3298501, 11 pages
https://doi.org/10.1155/2022/3298501

Research Article

Sources of Forecast Errors for Rainstorms in the South China Monsoon Region

Lin Lin,[1,2] **Chuhan Lu**,[1] **and Feifan Zhou**[2,3]

[1]*Key Laboratory of Meteorological Disaster, Ministry of Education/Joint International Research Laboratory of Climate and Environment Change/Collaborative Innovation Center on Forecast and Evaluation of Meteorological Disasters, Nanjing University of Information Science and Technology, Nanjing 210044, China*
[2]*Laboratory of Cloud–Precipitation Physics and Severe Storms (LACS), Institute of Atmospheric Physics, Chinese Academy of Sciences, Beijing 100029, China*
[3]*University of Chinese Academy of Sciences, Beijing 100049, China*

Correspondence should be addressed to Feifan Zhou; zhouff04@163.com

Received 3 September 2021; Accepted 22 January 2022; Published 26 March 2022

Academic Editor: Ismail gultepe

The possible sources of forecast errors associated with rainstorms in the South China monsoon region were investigated based on Weather Research and Forecasting (WRF) model forecasts for 19 rainstorm cases that occurred in the past 13 years. Two datasets were separately selected as the initial fields of WRF with the same physical parameterization schemes. By investigating the improvement rate of the forecast when using one set of data rather than the other, the important degree of the initial conditions with respect to the forecasts for each case has been obtained. For those initial errors are the important sources of forecast errors, we further explored the source of the initial errors by comparing the two initial conditions. It was found that, interestingly, the significant differences between two initial conditions are all located upstream the rainfall area, with a distance of 5° of longitude away and an area of about $4^\circ \times 4^\circ$. Based on this, we developed a new method (which we refer to as the "guide flow method") to identify the sensitive area for rainstorm forecasts in the South China monsoon region and then examined the efficiency of the sensitive areas. It was found that reducing the initial errors in the sensitive areas leads to better forecast results than doing the same in other areas. Thus, the sensitive areas are the source areas of forecast errors for rainstorms in the South China monsoon region.

1. Introduction

South China is affected by both the tropical and subtropical monsoon, in which the rainstorm process is closely related to the circulation of the summer monsoon [1, 2]. Rainstorms are one of the most serious types of natural disasters in South China [3–5]. However, currently, most global numerical models still carry considerable uncertainty in their forecasting of the location and precipitation amount of rainstorms [6, 7]. In particular, the forecasting of rainstorms in the South China monsoon region has always been a difficult and challenging issue in China's operational forecasting sector [8–10].

In recent years, most researchers have tended to focus on the underlying physical mechanisms of rainstorms in the South China monsoon region. Some of these studies have found that, during the active period of the summer monsoon, the South China Sea summer monsoon can extend to the rainstorm area in the form of low-frequency oscillations, and the rainstorm process has a good correlation with the pulsation or strengthening period of the monsoon [2]. After the onset of the summer monsoon, the Bay of Bengal and the Indian Ocean contribute significantly to the quantity of water vapor in South China [11]. Moreover, both the average precipitation and the convection intensity in South China have generally increased, and the convection intensity is basically consistent with the subseasonal changes in atmospheric thermodynamic conditions, which probably leads to the occurrence of regional extreme precipitation [12, 13]. For example, two strong rainstorms in Dongguan in July

2011 were caused by the onset of the southwest monsoon, the northward uplift of the ITCZ, and the pressure of the high-altitude East Asian trough [14].

In addition to the direct influence of summer monsoon circulation on precipitation, the rainstorm process in the South China monsoon region is also closely related to the prevailing mesoscale system under the influence of the summer monsoon [15]. For instance, the rainstorms on 11 May 2014, 19 May 2015, and 27 August 2018 were all caused by one or more mesoscale convective systems [16–19]. The evolution of the monsoon low-pressure intensity is synchronized with the daily distribution of the rainstorm area's size but not completely synchronized with the maximum daily precipitation's day-to-day evolution [17].

To study the predictability of rainstorms in the South China monsoon region, it is not enough just to understand the underlying physical mechanism of the rainstorm process; studying the forecast error of the numerical model is also necessary [20–23]. With continuous improvement in model accuracy, increasing the horizontal resolution of the model may improve the effects of the precipitation forecast [24–26]. Nevertheless, high-resolution models are still unable to reasonably reproduce the characteristics of the precipitation's distribution owing to the inherent unpredictability of the atmosphere, the imperfection of the numerical method in the dynamic framework of the physical processes, and so on, meaning current numerical precipitation forecasts usually carry large uncertainty [27].

In 2013, the China Meteorological Administration initiated the South China Monsoon Precipitation Experiment, which included studies on improving models and their initial fields [28–30]. Several researchers have found that improving the initial value assimilation technology of wind profile data can better describe the development of the convective system. Additionally, improvement of the low-level water vapor and wind field in the Weather Research and Forecasting (WRF) model data assimilation system can reduce the forecast error of heavy rain, thereby improving the prediction skill [31]. With the occurrence and development of precipitation, the evolution of errors gradually develops from local growth to global propagation, and the initial error in the precipitation area makes an important contribution to the precipitation forecast error [32]. A number of researchers have also studied the sensitivity of physical parameters and related conditional nonlinear optimal disturbances in the Global/Regional Assimilation and Prediction System for the forecasting of heavy rain in South China [33]. For instance, Lu et al. [34] studied a case of heavy rain in the South China monsoon region in 2015 and found that the initial error was an important source of forecast error, and the sensitive area could be found more accurately by the moist energy of perturbations.

Despite the clear need to explore the sources of error in rainfall forecasts in the South China monsoon region, there have been relatively few studies in this regard and so further exploration is still required. The present reported research sought to address this knowledge gap by developing a guide flow method to identify the sensitive area for rainstorm forecasts in this region. The overarching aim was to strengthen our understanding of the source areas of forecast error and improve the forecasting ability in the South China monsoon region.

2. Materials and Methods

2.1. Data and Study Area. Nineteen heavy rainstorm cases in South China in the past thirteen years that were mainly a result of the summer monsoon (rather than typhoons, etc.) were selected. In terms of observational data, the hourly precipitation gridded dataset (version 1.0) of the Chinese automatic station combined with the CMORPH (Climate Prediction Centre morphing technique) precipitation product (https://data.cma.cn/data/detail/dataCode/SEVP_CLI_CHN_MERGE_CMP_PRE_HOUR_GRID_0.10/keywords/CMORPH.html) was selected (hereinafter referred to as OBS). Besides, China Ground International Exchange Station daily climate data (http://data.cma.cn/data/cdcdetail/dataCode/SURF_CLI_CHN_MUL_DAY_CES_V3.0.html) were used to assist in screening the precipitation cases. The observed cumulative precipitation and distribution during the precipitation period of these cases are given in Table 1. From the data in Table 1, the daily mean maximum site precipitation of the selected 19 cases is 83.35 mm. Details of the different datasets used in the present study are given below.

NCEP_FNL (Final Global Data Assimilation System of the National Centers for Environmental Prediction) analysis data with a spatial resolution of 1.0° were used to generate the input field of the WRF model. According to Huang and Luo's [13] analysis of the five-day precipitation forecasts in three seasons (2013–2015) in South China, the European Centre for Medium-Range Weather Forecasts (ECMWF) model generally has high forecasting skill. Therefore, it can be assumed that both the initial field and the model of ECMWF have high accuracy. The ECMWF output (obtained from the TIGGE (THORPEX Interactive Grand Global Ensemble) dataset of the ECMWF center, hereinafter referred to as TIGGE_EC) was used as a control group with a spatial resolution of 0.5° latitude by 0.5° longitude. The initial conditions of TIGGE_EC were used to generate accurate initial conditions for the WRF forecasts.

2.2. WRF. Version 3.6.1 of WRF was employed in the present study. Both the initial fields and boundary fields were generated using FNL analysis data with a time interval of six hours. The horizontal resolution of the forecast was 3 km, with 1100×700 grid points, covering the entire South China region. Moreover, there were 60 layers in the vertical direction and the integration time step was 15 s without nesting. The physical parameterizations were as follows: Thompson scheme for the microphysical scheme; Goddard shortwave scheme for the shortwave radiation scheme; Rapid Radiative Transfer Model scheme for the longwave radiation scheme; Eta Mellor-Yamada-Janjic TKE (turbulent kinetic energy) scheme for the boundary layer; and the land surface process scheme adopted the Noah land surface model scheme, without cumulus parameterization [16, 34].

Table 1: Details of the cases used, including the time period, distribution, and cumulative amount of precipitation.

Case	Precipitation period	Precipitation distribution	Maximum site precipitation (mm)	Measured cumulative precipitation (mm)
1	2008.6.8(00 : 00)–6.9(00 : 00)	Central and western south China	164.9	582967.4
2	2008.6.11(00 : 00)–6.13(00 : 00)	Central and eastern south China	297.9	698194.2
3	2010.5.31(00 : 00)–6.2(00 : 00)	Central south China	87.0	983323.4
4	2011.6.28(00 : 00)–6.30(00 : 00)	Central and southern south China	448.5	506162
5	2011.7.15(00 : 00)–7.17(00 : 00)	Eastern south China	134.2	477601.5
6	2013.5.14(00 : 00)–5.17(00 : 00)	Central and eastern south China	195.3	705305.8
7	2013.7.26(00 : 00)–7.28(00 : 00)	Southern south China	189.3	567458.6
8	2014.5.21(12 : 00)–5.23(12 : 00)	Eastern south China	115.7	775429.6
9	2015.5.16(00 : 00)–5.17(00 : 00)	Southern and eastern south China	140.3	155520.7
10	2015.5.22(00 : 00)–5.23(00 : 00)	Southern south China	62.9	470785.5
11	2016.6.14(00 : 00)–6.15(00 : 00)	Eastern south China	68.7	238642
12	2017.5.14(00 : 00)–5.16(00 : 00)	Southeast of south China	106.5	277531.8
13	2017.6.4(00 : 00)–6.6(00 : 00)	Northeast of south China	106.7	293025.2
14	2017.7.2(00 : 00)–7.4(00 : 00)	Southern south China	246.2	294511.5
15	2018.4.15(00 : 00)–4.17(00 : 00)	Southern and eastern south China	—	45559.25
16	2018.5.7(00 : 00)–5.8(00 : 00)	Southern and eastern south China	115.1	106109.9
17	2018.5.9(00 : 00)–5.10(00 : 00)	Central south China	94.4	92764.41
18	2019.4.11(00 : 00)–4.12(12 : 00)	Southeast of south China	87.8	82066.8
19	2019.4.23(12 : 00)–4.25(00 : 00)	Central and eastern south China	43.9	86832.09

The forecasts using the WRF model initialized by NCEP_FNL data are denoted as WRF_FNL, while TIGGE_EC is used as a control group to be compared with WRF_FNL and OBS. Besides, we used accurate initial conditions (namely, the initial conditions of the TIGGE_EC forecasts) as the input field to generate the WRF forecasts (hereinafter referred to as WRF_EC) under the same physical parameterization schemes as WRF_FNL.

2.3. Methods. In order to comprehensively investigate forecast accuracy, namely, the similarity in the location and intensity between the forecast and observed cumulative precipitation in South China, the correlation coefficient was calculated as follows [35]:

$$r(F,O) = \frac{\operatorname{cov}(F,O)}{\sqrt{\operatorname{Var}[F] + \operatorname{Var}[O]}}, \quad (1)$$

where F is the forecast cumulative precipitation (TIGGE_EC, WRF_FNL or WRF_EC) in South China, O is the observed cumulative precipitation in South China, $r(F,O)$ is the correlation coefficient between F and O, cov(F, O) is the covariance of F and O, Var[F] is the variance of F, and Var [O] is the variance of O.

Besides, the grid-to-grid threat score (T_S) was calculated to investigate the forecasting of rainstorm events for different levels of precipitation, namely, light rain and heavy rain. T_S was calculated as follows [36]:

$$T_S = \frac{N_A}{N_A + N_B + N_C}, \quad (2)$$

where N_A represents the number of grid points where the forecast and observed precipitation are at the same level as light rain or (or heavy rain) and above, N_B is the number of grid points where the forecast precipitation level is light rain (or heavy rain) and above but observed precipitation is not at this level, and N_C is the number of grid points where light rain (or heavy rain) has not been forecast.

Since we found that improving the accuracy of the initial conditions could significantly improve the WRF model's forecasts, it is interesting to further explore the sources of initial errors. In this aspect, we compared the differences between the two kinds of initial conditions (FNL and EC) and calculated the vertical integration of moist energy of the differences. The idea is that the area of large moist energy will indicate where the large differences exist, and thus it is taken as the source area of the initial error [34, 37, 38].

The formula of moist energy is as follows [34]:

$$J = \int_0^1 \left[u_0'^2 + v_0'^2 + \frac{c_p}{T_r} T_0'^2 + R_a T_r \left(\frac{p_{S0}'}{pr} \right)^2 + \frac{L^2}{c_{pT_r}} q_0'^2 \right] \mathrm{d}\sigma, \quad (3)$$

where σ is the vertical coordinate; C_p is the specific heat at constant pressure (= 1005.7 J kg^{-1}·K^{-1}); R_a is the dry air gas constant (=287.04 J·kg^{-1}·K^{-1}); p_r = 1000 hPa; T_r = 270 K; and u_0', v_0', T_0', p_{s0}', and q_0' are the differences in meridional wind, zonal wind, temperature, surface pressure, and water vapor mixing ratio between the EC and FNL initial fields, respectively. Compared with a single variable, moist energy indicates the comprehensive influence of all variables. Lu et al. [34] found that moist energy could help screen out the source area of the initial error, and the improvement of the initial conditions in that source area could achieve the greatest benefits compared to the improvement of initial conditions in other areas. Thus, hereafter, we refer to this method as the "moist energy method," and the source area as the "sensitive area."

3. Results

In 73.7% (14 cases) of the 19 cases, the correlation coefficient between TIGGE_EC and OBS is higher than that between WRF_FNL and OBS, and the average correlation between TIGGE_EC and OBS of the 19 cases is 0.428, which is significantly higher than that between WRF_FNL and OBS (0.328). Besides, the shaded area of the correlation coefficient in Figure 1 shows the extent to which TIGGE_EC is better than WRF_FNL.

Comparison of the cumulative precipitation distribution of WRF_FNL, TIGGE_EC, and OBS in cases 4 and 9 shows that WRF_FNL and TIGGE_EC differ in precipitation intensity and location compared with OBS (Figure 2). However, both the intensity and location of the precipitation forecast by TIGGE_EC are more similar than those of WRF_FNL to OBS. TIGGE_EC has a better effect on the forecasting of the precipitation center in southwest Guangdong and southern Guangxi in both case 4 and case 9. Combined with Figure 1, it can be seen that TIGGE_EC is closer to OBS than WRF_FNL and has a better forecast result, which is consistent with the findings of Huang and Luo [13]. Therefore, in these 14 cases, we assume that both the initial field and the model (i.e., the ECMWF model) have high accuracy, and we only examine these 14 cases in the following parts.

Next, we used accurate initial conditions (namely, those of TIGGE_EC forecasts) to generate WRF forecasts (hereafter referred to as WRF_EC) for the 14 cases in which the forecast of TIGGE_EC was better than WRF_FNL and quantitatively compared them with WRF_FNL. First, the TIGGE_EC forecasts were taken as the true values to examine the improvements in forecasts when using accurate initial conditions. It was found that the average correlation between the cumulative precipitation in South China forecast by WRF_EC and TIGGE_EC is 0.430, which is higher than that between the forecasts of WRF_FNL and TIGGE_EC (0.390).

Meanwhile, 71.4% of the 14 cases have better forecast skill with WRF_EC than with WRF_FNL. Taking case 9 as an example, it can be seen that both the location and the intensity of the precipitation forecasted by WRF_EC are closer to those of TIGGE_EC than WRF_FNL (Figure 2). Arguably, however, although the TIGGE_EC forecasts appear to be more accurate than the WRF_FNL forecasts, they still contain errors. Thus, we further used OBS as the true values to evaluate the improvements of WRF_EC compared to WRF_FNL, and the results turned out to be similar. That is, the cumulative precipitation in South China of OBS generally has higher correlation coefficients with WRF_EC than with WRF_FNL (Table 2). In other words, WRF_EC generates precipitation patterns that are more similar to OBS compared to WRF_FNL.

Besides, we also checked the T_s scores of WRF_EC and WRF_FNL; here, the OBS are used as true values. From Table 3, we can see that, of the 14 cases, there are, respectively, 8 cases and 10 cases for which WRF_EC has better T_s than WRF_FNL for "light rain and above" and "heavy rain and above" (Table 3). This indicates that WRF_EC generates precipitation amounts that are more similar to OBS than WRF_FNL.

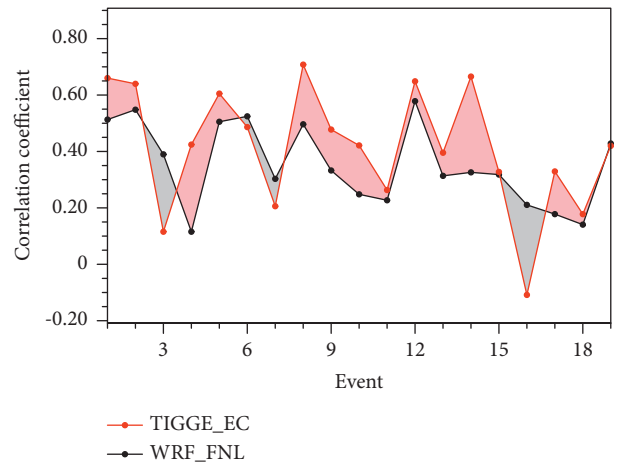

Figure 1: Correlation with OBS of the cumulative precipitation forecast by WRF_FNL (black) and TIGGE_EC (red).

From the above results, it is seen that forecasts of WRF_EC are better than those of WRF_FNL as regards both the precipitation patterns and precipitation amounts. In short, the WRF_EC forecasts are better than the WRF_FNL forecasts.

By quantitatively investigating the improvement in the forecast, we can examine the importance of the accuracy of the initial conditions in the forecasts and thus judge the source of the forecast errors for summer rainstorms in South China. Therefore, we define the following parameters:

$$\mathrm{IM}_1 = \frac{O_{\mathrm{EC}} - O_{\mathrm{FNL}}}{O_{\mathrm{FNL}}},$$
$$\mathrm{IM}_2 = \frac{T_{\mathrm{EC}} - T_{\mathrm{FNL}}}{T_{\mathrm{FNL}}}. \tag{4}$$

Here, O_{FNL} is the correlation between the cumulative precipitation in South China of WRF_FNL and OBS, while O_{EC} is the same but between WRF_EC and OBS. Similarly, T_{FNL} represents the correlation between WRF_FNL and TIGGE_EC, while T_{EC} represents the correlation between WRF_EC and TIGGE_EC. Then, we define the degree of improvement with IM_1 and IM_2 for each case. If IM_1 (IM_2) $\geq 50\%$, improving the initial value can significantly improve the forecast, and therefore the initial error is the main source of forecast errors. We define such a degree of improvement as "significantly improved." In this category, there are six cases, accounting for 31.6% of all cases. Likewise, if $0 < \mathrm{IM}_1$ (IM_2) $< 50\%$, then improving the initial value can slightly improve the forecast (thus defined as "slightly improved"), for which there are four cases, accounting for 21.1% of all cases. Lastly, if IM_1 (IM_2) < 0, improving the initial value can barely improve the forecast results, and so the degree of improvement is defined as "not improved," for which there are also four cases. The IM_1 and IM_2 values for the above 14 cases are shown in Table 4.

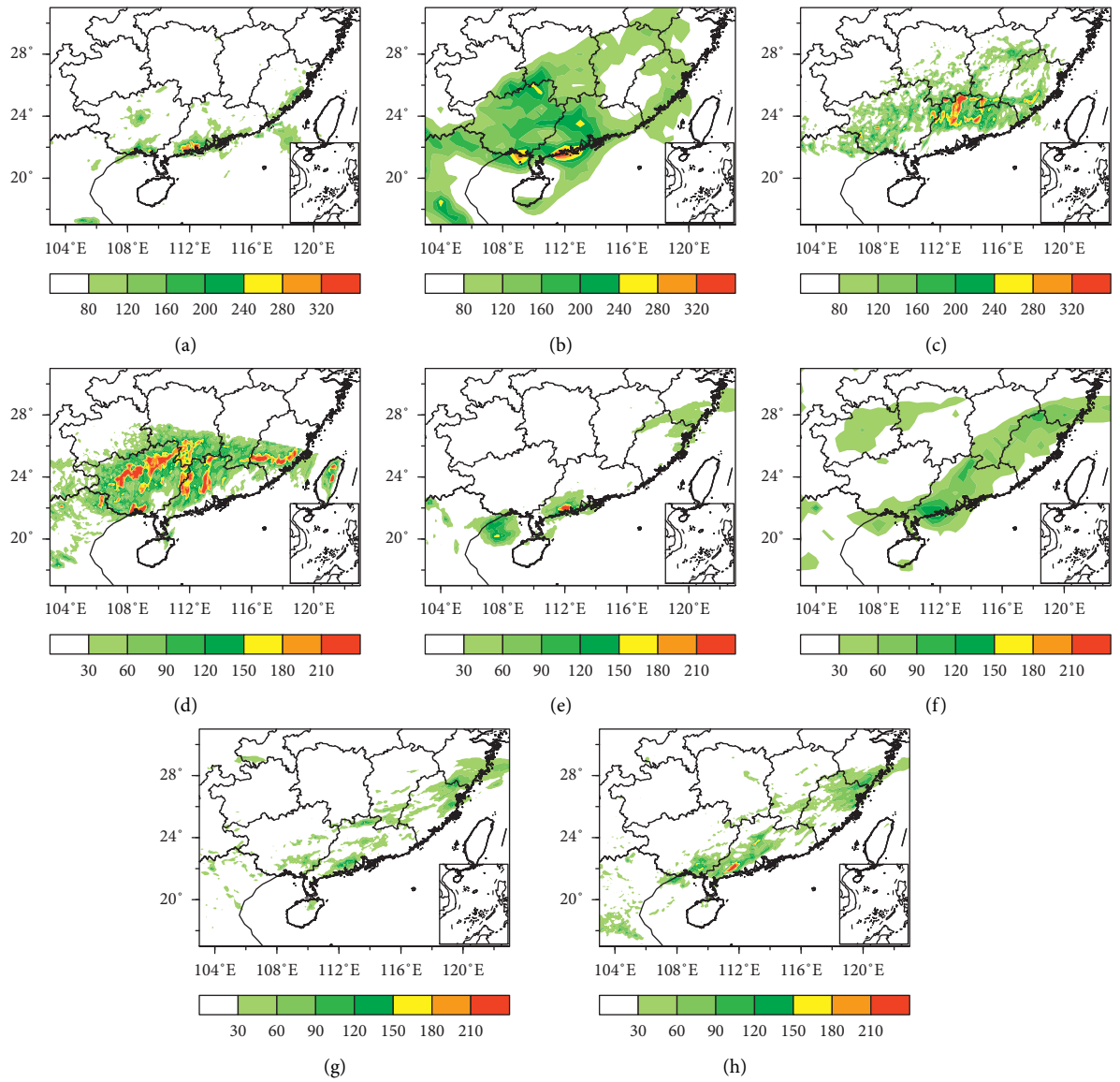

Figure 2: Cumulative precipitation (unit: mm) distribution of ((a) and (e)) OBS, ((b) and (f)) WRF_FNL, ((c) and (g)) TIGGE_EC, and ((d) and (h)) WRF_EC in ((a)–(d)) case 4 and ((e)–(h)) case 9.

According to Table 4, the 14 cases can be divided into three types: "significantly improved," "slightly improved," and "not improved." It is seen that, among the 14 cases, the forecasts of 6 cases are significantly improved after improving the initial field, For those slightly improved cases, the initial errors also play some parts in the forecast errors, so it is also meaningful to explore the source of the initial errors for those cases. Thus, next step, we explore the source of the initial errors for the "significantly improved" group and the "slightly improved" group (a total of 10 cases).

The differences between two kinds of initial conditions are explored, and the area of largest differences is taken as the source area (also called sensitive areas hereafter) of the initial errors. By analyzing the basic flows at 700 hPa, we found that the sensitive areas are located in the basic flows that are directed towards the precipitation area. This means that the initial errors mainly come from upstream the precipitation area. To quantitatively find out the relationship between the precipitation area and the sensitive area, we selected both their sizes as $4^\circ \times 4^\circ$ (Figure 3) and found that their distances are about 5° of longitude. Based on the above results, we developed a method to identify the sensitive area by combining the precipitation area and the basic state wind (hereafter referred to as the "guide flow method"). The precipitation area is centered on the maximum precipitation point. First, we define the direction of the guide flow at 700 hPa as follows:

$$\tan(\theta) = \frac{v}{u} = \frac{\text{lat}}{\text{lon}}, \tag{5}$$

where u and v are the zonal and meridional wind components on 700 hPa, respectively; θ is the angle between the wind direction at 700 hPa and the horizontal direction. lat is

Table 2: Correlation coefficients of WRF_FNL and WRF_EC with both OBS and TIGGE_EC for cumulative precipitation in South China.

Case	Correlation coefficient (with OBS)		Correlation coefficient (with TIGGE_EC)	
	WRF_FNL	WRF_EC	WRF_FNL	WRF_EC
1	0.512974	0.607617	0.486501	0.643501
2	0.548051	0.174862	0.5627	0.177614
4	0.115652	0.42435	0.28005	0.369751
5	0.505295	0.537231	0.560114	0.597676
8	0.496311	0.46829	0.647559	0.540012
9	0.332558	0.363309	0.437344	0.487258
10	0.062397	0.248002	0.279877	0.290106
11	0.226967	0.305981	0.188803	0.340021
12	0.578311	0.532898	0.444847	0.349342
13	0.313502	0.326267	0.250141	0.271314
14	0.325913	0.393516	0.325419	0.499911
15	0.318089	0.447602	0.204124	0.408888
17	0.177811	0.329199	0.321906	0.501076
18	0.140593	0.070364	0.140593	0.393925

Table 3: T_S of WRF_FNL and WRF_EC with respect to OBS in the 14 cases (T_S of WRF_EC marked in red has better forecast).

Case	T_S (light rain and above)		T_S (heavy rain and above)	
	WRF_FNL	WRF_EC	WRF_FNL	WRF_EC
1	0.212	0.405	0.189	0.311
2	0.417	0.170	0.356	0.123
4	0.166	0.200	0.088	0.094
5	0.292	0.318	0.088	0.266
8	0.296	0.286	0.114	0.134
9	0.241	0.350	0.088	0.014
10	0.29	0.286	0.28	0.223
11	0.193	0.200	0	0
12	0.202	0.210	0.045	0.054
13	0.346	0.310	0.061	0.091
14	0.230	0.242	0.161	0.202
15	0.411	0.377	0.063	0.071
17	0.210	0.271	0.008	0.015
18	0.065	0.032	0.010	0.012

Table 4: Classification of IM_1 and IM_2 and the degree of improvement corresponding to each case.

Case	IM_1	IM_2	Degree of improvement
1	0.184498	0.322713	Slightly improved
2	−0.68094	−0.68435	Not improved
4	0.906682	0.320304	Significantly improved
5	0.063203	0.067061	Slightly improved
8	−0.05646	−0.16608	Not improved
9	0.092468	0.11413	Slightly improved
10	2.974582	0.036548	Significantly improved
11	0.348127	0.80093	Significantly improved
12	−0.07853	−0.21469	Not improved
13	0.04072	0.084644	Slightly improved
14	0.207425	0.536207	Significantly improved
15	0.407161	1.003135	Significantly improved
17	0.851398	0.556591	Significantly improved
18	−0.998083	0.643097	Not improved

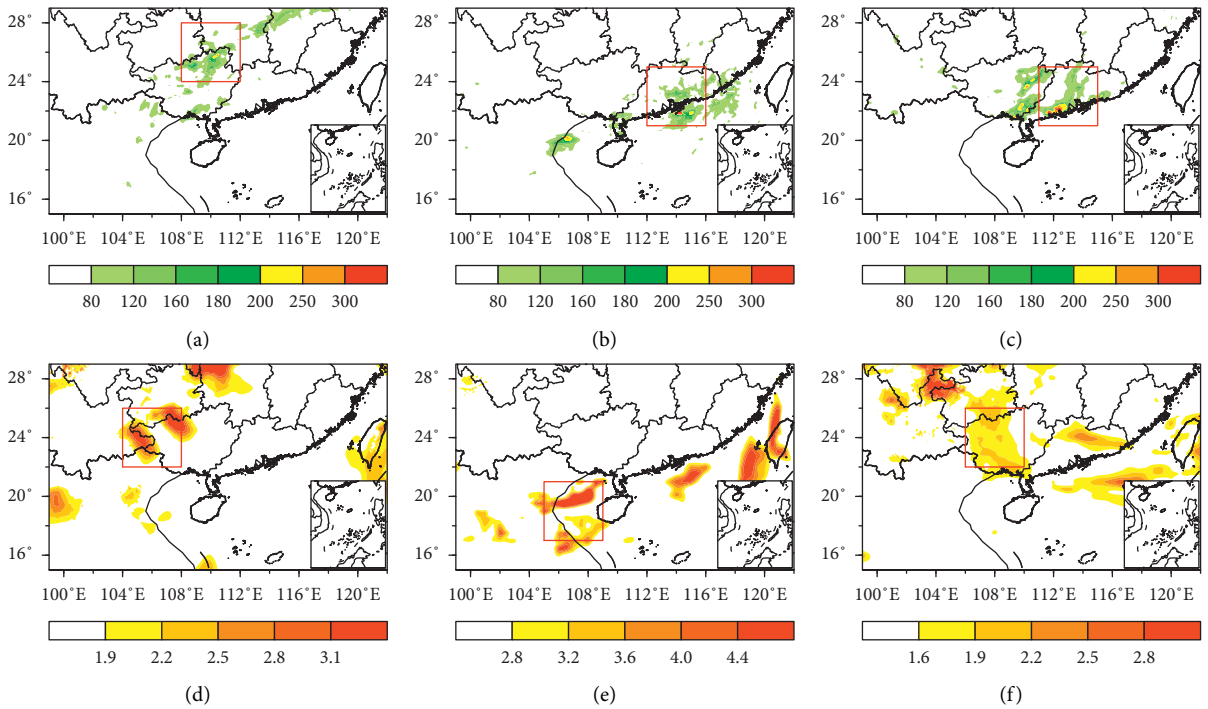

Figure 3: ((a)–(c)) Distribution of cumulative precipitation (unit: mm) in cases 1, 5, and 14, respectively (the red box is the range of the precipitation area selected). ((d)–(f)) The sensitive areas selected with the moist energy (unit: 1×10^5 J) method for cases 1, 5, and 14, respectively (the red box is the range of the sensitive area selected).

the latitudinal difference between the maximum precipitation point and the selected maximum point of the sensitive area; lon = 5°, which is the longitudinal difference between the maximum precipitation point and the selected maximum point of the sensitive area. From the description above, u, v, and lon are all known, and then lat can be derived. Thus, the sensitive area can be determined according to the precipitation area, $\tan(\theta)$, and the lat and lon values.

If the guide flow in the precipitation area is relatively straight, then u and v are the zonal and meridional wind components of the maximum precipitation point. With lon known and $\tan(\theta)$ obtained by linear backward deduction of the wind (u and v) in the precipitation area, lat can be derived, so the sensitive area can be determined (Figure 4(a)). If there are obvious troughs or cyclonic circulations in the precipitation area, u and v are the average zonal and meridional wind components of the precipitation area. Similarly, the location of the sensitive area can be deduced according to the average guide flow direction in the precipitation area (Figure 4(b)). Whether the guide flow is relatively straight or there are obvious troughs or cyclonic circulations in the precipitation area, the sensitive area selected by the guide flow method is relatively consistent with the location of the large-value area of moist energy (Figure 4).

Table 5 shows the locations of the sensitive areas determined by the guide flow method and the moist energy method. For 80% (8 cases) of the 10 cases, the positions of the sensitive areas selected by the two methods are relatively consistent, with the distances between them being less than 2°. Thus, the sensitive area selected by the guide flow method is similar to that identified by the moist energy method. To confirm this point, we also use both the guide flow method and the moist energy method to identify the sensitive areas of those cases that belong to "not improved" group (cases 2, 8, 12, and 18) in Table 4 and those cases where TIGGE_EC has lower skills than WRF_FNL (cases 3, 6, 7, 16, and 19) in Figure 1. Results showed that, for 8 out of 9 cases, the positions of the sensitive areas selected by the two methods are similar (Table 6). This confirms that the guide flow method can be used to identify sensitive areas associated with rainstorm forecasts. Since the guide flow method is easy to use, it thus may be helpful for quickly selecting perturbation areas for ensemble forecasts or carrying out supplemental observations for adaptive observations.

To verify the accuracy of the sensitive areas, namely, to demonstrate that they are the source areas of the initial errors which lead to large forecast errors, we chose three other areas for comparison and carried out sensitivity experiments. These three areas had the same size as sensitive areas, and they were, respectively, located to the west, south, and north of the precipitation areas with distances of 10° longitude, 5° latitude, and 5° latitude. Then, the initial conditions of WRF_FNL were replaced with those of WRF_EC in the sensitive area to form new ones. Similarly, three other sets of new initial conditions were generated by replacing those of WRF_FNL with the initial conditions of WRF_EC in those three areas.

Keeping the model configuration unchanged, four new forecasts were produced with the above four sets of new initial conditions, and these are, respectively, referred to here

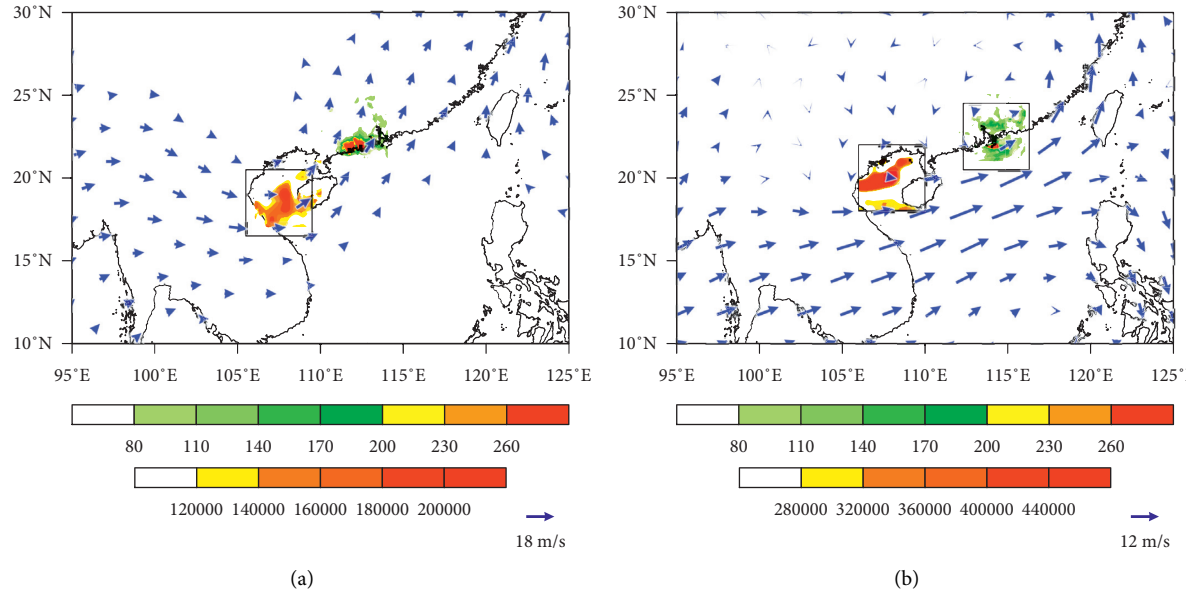

Figure 4: Sensitive area selected with the guide flow method (rectangles in panel (a) and left rectangles in panel (b)), sensitive areas identified by moist energy (unit: 1×10^5 J the left parts of shadings in both two panels), and the precipitation area (unit: mm, the right parts of shadings in both two panels) overlayed with the 700 hPa wind field in (a) case 4 and (b) case 5.

Table 5: Comparison of sensitive areas selected with moist energy method and guide flow method.

Case	Sensitive areas selected with the moist energy method	Sensitive areas selected with guide flow method
1	(22°–26°N, 104°–108°E)	(21°–25°N, 103°–107°E)
4	(16°–20°N, 107°–111°E)	(16°–20°N, 106°–110°E)
5	(18°–22°N, 105°–109°E)	(18°–22°N, 106°–110°E)
9	(20°–24°N, 104°–108°E)	(18°–22°N, 105°–109°E)
10	(18°–22°N, 106°–110°E)	(18°–22°N, 107°–111°E)
11	(12°–16°N, 102°–106°E)	(21°–25°N, 102°–106°E)
13	(17°–21°N, 104°–108°E)	(18°–22°N, 102°–106°E)
14	(20°–24°N, 105°–109°E)	(16°–20°N, 105°–109°E)
15	(20°–24°N, 107°–111°E)	(21°–25°N, 106°–110°E)
17	(20°–24°N, 106°–110°E)	(19°–23°N, 105°–109°E)

Table 6: Same as Table 5 but for verifying cases.

Case	Sensitive areas selected with the moist energy method	Sensitive areas selected with guide flow method
2	(17°–21°N, 103°–107°E)	(20°–24°N, 103°–107°E)
3	(15°–19°N, 100°–104°E)	(13°–17°N, 102°–106°E)
6	(20°–24°N, 106°–110°E)	(21°–25°N, 107°–111°E)
7	(14°–18°N, 99°–103°E)	(19°–23°N, 102°–106°E)
8	(20°–24°N, 105°–109°E)	(18°–22°N, 106°–110°E)
12	(21°–25°N, 107°–111°E)	(19°–23°N, 106°–110°E)
16	(21°–25°N, 106°–110°E)	(21°–25°N, 109°–113°E)
18	(22°–26°N, 105°–109°E)	(22°–26°N, 106°–110°E)
19	(24°–28°N, 105°–109°E)	(23°–27°N, 104°–108°E)

as F-sens, F-north, F-west, and F-south. The cumulative precipitation of these forecasts was compared with the observed precipitation in South China, and their correlation coefficients were calculated. It can be seen from the results (Figure 5) that, for the 10 improved cases in Table 4, there are 9 cases where the correlations between F-sens and OBS are

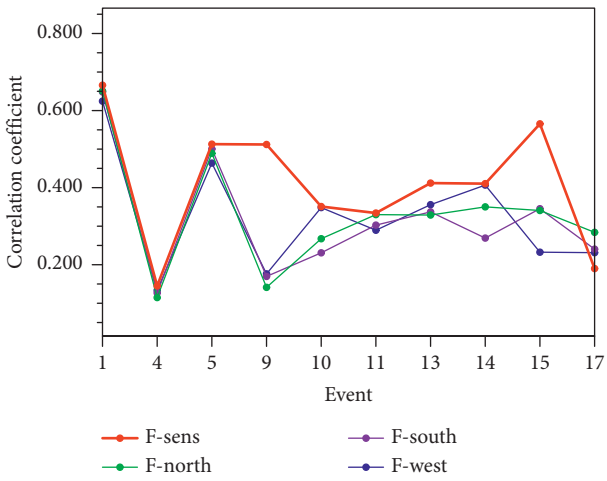

Figure 5: Sensitivity experiment results of 10 improved cases in Table 4, in which the red, green, purple, and blue lines plot the correlation coefficients between the cumulative precipitation results after replacing the sensitive area, northern control area, southern control area, western control area, and OBS in South China, respectively.

higher than other correlations (F-north and OBS, F-west and OBS, and F-south and OBS). This means that improving the initial conditions in sensitive areas can improve the forecast to a greater extent than by improving them in other areas, and again this verifies that the sensitive areas are the source areas of initial errors as well as the forecast errors.

4. Conclusion

Based on the WRF model, this paper has investigated the possible sources of forecast errors with respect to rainstorms in the South China monsoon region. First it is demonstrated that the initial error is the important source of the forecast errors, and then the source area (sensitive area) of initial errors is explored. Next, the relationship between the sensitive area and the precipitation area is analyzed. Based on the above results, a new method is developed (which we call the "guide flow method") to identify the sensitive area. Finally, the sensitive areas were examined through sensitivity experiments, which confirmed the accuracy of the sources of initial errors as well as the forecast errors.

By investigating the improvement rate of the forecast when using one set of data rather than the other, the important degree of the initial conditions with respect to the forecasts for each case has been obtained. The results showed that forecasts of 6 cases have been significantly improved (the improvement rate is larger than 0.5), which means that, for these cases, the initial condition plays a main role in the forecasts. While the forecasts of 4 cases have been slightly improved, this means the initial condition also has some effects on the forecasts. For these 10 cases, the initial errors are the important sources of forecast errors; then we further explored the source of the initial errors by comparing the two initial conditions. The results showed that the initial errors mainly came from an area located upstream of the rainfall area (about 5° of longitude away from the maximum precipitation area) and we called that area the sensitive area. By studying the relationship between the sensitive area and the precipitation area, we found out the rules behind it and then put forward a "guide flow" method to identify the sensitive areas. The sensitive areas identified by the guide flow method were found to be generally consistent with those identified by the moist energy method. Since the guide flow method is easy to use, it thus may be helpful for quickly selecting perturbation areas for ensemble forecasts or carrying out supplemental observations for adaptive observations. Finally, sensitivity experiments demonstrated that improving the initial conditions in the sensitive areas leads to more benefits than improving them in other same-sized areas. This verifies the accuracy of the sensitive areas and confirms the source of the forecast errors.

Statistically, improving the initial conditions may improve the forecasting of rainstorms in the South China monsoon region. However, there are some cases (such as the 2019.4.12 case) in which improving the initial conditions has no benefit on the forecasts. Thus, for these cases, the model error has an important impact on the rainstorm forecast. Besides, there are some cases where we fail to find a better initial condition (cases 3, 6, 7, 16, and 19); for these cases, it is necessary to find out other ways to evaluate the importance of the initial conditions. In a word, in order to further improve the prediction skill for rainstorms in the South China monsoon region, further in-depth research is still needed.

Data Availability

The data used in this paper can be obtained from Lin Lin (20211101017@nuist.edu.cn) upon request.

Conflicts of Interest

The authors declare that they have no conflicts of interest regarding the publication of this paper.

Acknowledgments

The authors express their appreciation to the staff at the China Meteorological Data Service Centre and those involved in the Final Global Data Assimilation System and the THORPEX Interactive Grand Global Ensemble from the ECMWF. This research was funded by the National Key Research and Development Program of China (Grants 2018YFC1507405 and 2017YFC1501601).

References

[1] T. J. Zhou and R. C. Yu, "Atmospheric water vapor transport associated with typical anomalous summer rainfall patterns in China," *Journal of Geophysical Research: Atmospheres*, vol. 110, 2005.

[2] R. X. Liu, J. H. Sun, and B. F. Chen, "Selection and classification of warm-sector heavy rainfall events over South

China," *Chinese Journal of Atmospheric Sciences*, vol. 43, no. 1, pp. 122–133, 2019, in Chinese.

[3] M. Zhang and Z. Meng, "Impact of synoptic-scale factors on rainfall forecast in different stages of a persistent heavy rainfall event in south China," *Journal of Geophysical Research: Atmospheres*, vol. 123, no. 7, pp. 3574–3593, 2018.

[4] Q. Q. Li, G. H. Wang, S. Yang, and F. Wang, "Sub-seasonal prediction of rainfall over the South China Sea and its surrounding areas during spring–summer transitional season," *International Journal of Climatology*, vol. 40, no. 10, pp. 4326–4346, 2019.

[5] S. X. Zhong, S. Yang, C. Y. Guo, and Z. T. Chen, "Capabilities and limitations of GRAPES simulations of extreme precipitation in the warm sector over a complex orography," *Journal of Tropical Meteorology*, vol. 25, no. 2, pp. 42–53, 2019.

[6] Z. Li, Y. Luo, Y. Du, and J. C. L. Chan, "Statistical characteristics of pre-summer rainfall over south China and associated synoptic conditions," *Journal of the Meteorological Society of Japan. Series II*, vol. 98, no. 1, pp. 213–233, 2020.

[7] J. Du and J. Li, "Application of ensemble forecast method in the study and forecast of heavy rain," *Advances in Meteorological Science and Technology*, vol. 4, no. 5, pp. 6–20, 2014.

[8] T. Chen, J. Sun, Y. Chen, Y. C. Guo, and J. Xu, "Study on the numerical predictivity of localized severe mesoscale rainstorm in Guangzhou on 7 may 2017," *Meteorological Monthly*, vol. 45, no. 9, pp. 1199–1212, 2019, in Chinese.

[9] Y. Luo, R. Zhang, Q. Wan, B. Wang, and Y. Xiao, "The southern China monsoon rainfall experiment (SCMREX)," *Bulletin of the American Meteorological Society*, vol. 98, no. 5, 2016.

[10] Y. Luo, J. Sun, Y. Li et al., "Science and prediction of heavy rainfall over China: research progress since the reform and opening-up of new China," *Journal of Meteorological Research*, vol. 34, no. 3, pp. 427–459, 2020.

[11] Y. Chen and Y. Luo, "Analysis of paths and sources of moisture for the south China rainfall during the presummer rainy season of 1979-2014," *Journal of Meteorological Research*, vol. 32, no. 5, pp. 744–757, 2018.

[12] Y. Luo, H. Wang, R. Zhang, W. Qian, and Z. Luo, "Comparison of rainfall characteristics and convective properties of monsoon precipitation systems over south China and the yangtze and huai river basin," *Journal of Climate*, vol. 26, no. 1, pp. 110–132, 2013.

[13] L. Huang and Y. Luo, "Evaluation of quantitative precipitation forecasts by TIGGE ensembles for south China during the presummer rainy season," *Journal of Geophysical Research: Atmospheres*, vol. 122, no. 16, pp. 8494–8516, 2017.

[14] J. M. Zhang, W. Q. Mo, and J. Y. Yan, "Analysis of characteristics of two rounds of heavy rainfall in Dongguan under the background of southwest Monsoon onset," *Guangdong Meteorology*, vol. 36, no. 1, pp. 40–44+48, 2014, in Chinese.

[15] J. B. Lin, Y. T. Li, Y. N. Zheng, and H. Chen, "Analysis of a continuous rainstorm process of South China Monsoon low pressure," *Guangdong Meteorology*, vol. 41, no. 6, pp. 29–33, 2019, in Chinese.

[16] X. Liu, Y. Luo, Z. Guan, and D.-L. Zhang, "An extreme rainfall event in coastal south China during SCMREX-2014: formation and roles of rainband and echo trainings," *Journal of Geophysical Research: Atmospheres*, vol. 123, no. 17, pp. 9256–9278, 2018.

[17] J. J. Cai, Z. F. Wu, X. Q. Chen, Y. Lan, Z. Y. Guo, and C. Y. Guo, "An analysis of the causes of the "18·8" Guangdong monsoon low and sustained heavy rain," *Terminal Rain and Disasters*, vol. 38, no. 6, pp. 576–586, 2019, in Chinese.

[18] Z. Y. Guo, Z. F. Wu, J. J. Cai, H. L. Zhang, and X. Y. Chen, "Analysis of water vapor transport characteristics of a monsoon low-pressure continuous heavy rain event at the end of August 2018 in Guangdong area," *Torrential Rain and Disasters*, vol. 38, no. 6, pp. 587–596, 2019, in Chinese.

[19] Y. Shen, Y. Du, and G. X. Chen, "Ensemble sensitivity analysis of heavy rainfall associated with three MCSs coexisting over southern China," *Journal of Geophysical Research: Atmospheres*, vol. 125, no. 2, Article ID e2019JD031266, 2020.

[20] M. Mu, D. Wansuo, and C. Jifan, "Recent advances in predictability studies in China (1999-2002)," *Advances in Atmospheric Sciences*, vol. 21, no. 3, pp. 437–443, 2004.

[21] M. Mu, W. Duan, Q. Wang, and R. Zhang, "An extension of conditional nonlinear optimal perturbation approach and its applications," *Nonlinear Processes in Geophysics*, vol. 17, no. 2, pp. 211–220, 2010.

[22] Q. Wang, M. Mu, and H. A. Dijkstra, "Application of the conditional nonlinear optimal perturbation method to the predictability study of the kuroshio large meander," *Advances in Atmospheric Sciences*, vol. 29, no. 1, pp. 118–134, 2012.

[23] M. Mu and W. Duan, "Conditional nonlinear optimal perturbation and its applications to the studies of weather and climate predictability," *Chinese Science Bulletin*, vol. 50, no. 21, pp. 2401–2407, 2005.

[24] N. N Li, "Hourly refined evaluation of precipitation simulation in China," *Chinese Academy of Meteorological Sciences*, in Chinese, 2020.

[25] X. Li, L. F. Zhang, and J. N. Wang, "The sensitivity of the prediction of Meiyu torrential rainfall to model resolution and cumulus parameterization," *Torrential Rain and Disasters*, vol. 39, no. 6, in Chinese, Article ID 10, 2020.

[26] A. Fernández, V. Schumacher, I. Ciocca, A. Rifo, and F. Justino, "Validation of a 9-km WRF dynamical downscaling of temperature and precipitation for the period 1980–2005 over Central South Chile," *Theoretical and Applied Climatology*, vol. 143, no. 1-2, pp. 1–18, 2021.

[27] Z. H. Li and Y. L. Luo, "Statistical characteristics of presummer rainfall over South China before and after South China Sea monsoon onset from 1980 to 2017," *Torrential Rain and Disasters*, vol. 40, no. 2, Article ID 10, 2021.

[28] R. Zhang, Y. Ni, L. Liu, Y. Luo, and Y. Wang, "South China heavy rainfall experiments (SCHeREX)," *Journal of the Meteorological Society of Japan. Ser. II*, vol. 89A, no. 2, pp. 153–166, 2011.

[29] S. W. Li, S. Yang, and H. W. Liu, "Sensitivity of warm-sector heavy precipitation to the impact of anthropogenic heating in South China," *Atmospheric and Oceanic Science Letters*, vol. 11, no. 3, pp. 236–245, 2018.

[30] Y. Luo, L. Li, R. H. Johnson et al., "Science and prediction of monsoon heavy rainfall," *Science Bulletin*, vol. 64, no. 21, pp. 1557–1561, 2019.

[31] X. Zhang, Y. Luo, Q. Wan, W. Ding, and J. Sun, "Impact of assimilating wind profiling radar observations on convection-permitting quantitative precipitation forecasts during SCMREX," *Weather and Forecasting*, vol. 31, no. 4, pp. 1271–1292, 2016.

[32] Y. Luo and L. F. Zhang, "A case study of the error growth evolution in a meiyu front heavy precipitation forecast and an analysis of the predictability," *Acta Meteorologica Sinica*, vol. 68, no. 3, pp. 411–420, 2010.

[33] L. Wang, X. Shen, J. Liu, and B. Wang, "Model uncertainty representation for a convection-allowing ensemble prediction system based on CNOP-P," *Advances in Atmospheric Sciences*, vol. 37, no. 8, Article ID 15, 2020.

[34] C. H. Lu, L. Lin, and F. F. Zhou, "Analysis of the source of forecast errors for a heavy precipitation in the southwest of Guangdong province," *Chinese Journal of Atmospheric Sciences*, vol. 44, no. 6, in Chinese, Article ID 12, 2020.

[35] F. Y. Wei, *Modern Climate Statistics Diagnosis and Prediction Technology*, Second edition, Weather Press, Beijing, China, 2007, in Chinese.

[36] M. Y. Ding, L. L. Wang, Y. Xin et al., "TS score analysis of WRF cloud microphysical parameterization scheme on Xinjiang's rainstorm simulation ability," *Arid Zone Research*, vol. 36, no. 6, pp. 1411–1418, 2019.

[37] F. Zhou, M. Yamaguchi, and X. Qin, "Possible sources of forecast errors generated by the global/regional assimilation and prediction system for landfalling tropical cyclones. Part I: initial uncertainties," *Advances in Atmospheric Sciences*, vol. 33, no. 7, pp. 841–851, 2016.

[38] F. F. Zhou, W. Duan, H. Zhang, and M. Yamaguchi, "Possible sources of forecast errors generated by the global/regional assimilation and prediction system for landfalling tropical cyclones. Part II: model uncertainty," *Advances in Atmospheric Sciences*, vol. 33, no. 7, pp. 841–851, 2018.

Hindawi
Advances in Meteorology
Volume 2022, Article ID 9320089, 16 pages
https://doi.org/10.1155/2022/9320089

Research Article

Numerical Modeling the Flood and Pollutant Transport Processes in Residential Areas with Different Land Use Types

Shulin Fang,[1] Yongpeng Ji,[2] and Mingliang Zhang [2,3]

[1]*Dalian Marine Environment Monitoring Center Station, Dalian, Liaoning Province 116015, China*
[2]*School of Ocean Science and Environment, Dalian Ocean University, Dalian 116023, China*
[3]*State Key Laboratory of Coastal and Offshore Engineering, Dalian University of Technology, Dalian, China*

Correspondence should be addressed to Mingliang Zhang; zhmliang_mail@126.com

Received 16 April 2021; Revised 29 August 2021; Accepted 20 December 2021; Published 6 January 2022

Academic Editor: Gabriele Buttafuoco

Large-scale flooding causes widespread disaster, and harmful pollutant concentration in water following flood affects public safety and the environment. In this study, a numerical model for solving the 2D shallow water equations and the solute transport equation is proposed to simulate overland flood and pollutant transport caused by floods. The present model is verified by comparing the predictions with the analytical solutions and simulation results; sufficiently high computational accuracy is achieved. The model is also used to simulate flood inundation and pollution spread in the area of Hun and Taizi Lane (HTL) in China due to river dike breaches; the results show that the coupling model has excellent performance for simulating the flooding process and the temporal and spatial distribution of pollutants in urban or rural areas. We use remote sensing techniques to acquire the land coverage in the area of HTL based on Landsat TM satellites. The impacts of changed land use on mitigation of flooding waves and pollutant spread are investigated; the results indicate that the land cover changes have an obvious influence on the evolution process of flood waves and pollutant transport in the study areas, where the transport of pollutants is very dynamic during flood inundation in HTL area. Furthermore, the motion of pollutants considering anisotropic diffusion is more reasonable than that due to isotropic dispersion in simulating pollutant transport associated with the flood in urban or farmland environments.

1. Introduction

Floods are triggered by the rapid rise of the water level after heavy rainfall; they can cause the river to overflow the embankment, thereby increasing the flood risk in downstream and low-lying areas. Usually, urban environments and rural farmland are vulnerable to flood damage due to the high population density and large areas of crops. Up to now, many areas worldwide have suffered heavy rains and flood disasters. For example, in July 1982, Nagasaki in Japan suffered a massive flood after heavy rain, resulting in property losses of as much as $2.5 billion. In July 1995, the Hun River and Taizi River basins located in Liaoning Province in China experienced large flood events; multiple levees burst in both rivers and $7.6 \times 10^5\,\mathrm{hm}^2$ of farmland were submerged by the flood following a dike break; the economic losses reached ¥34.4 billion. The Brisbane River in Australia flooded after continuous rainfall in January 2011, resulting in a severe flood disaster with large impacts on urban residents and the infrastructure [1]. Flooding events in Europe caused losses of about 4.9 billion euros every year from 2000 to 2012 [2].

Numerous studies on flood inundation in a way can minimize the mitigation of negative consequences of flood events by predicting the movement characteristics of floods in [3, 4]. Several different types of models have been developed for flood hazard simulation and prediction in high-risk zones based on the rich floodplain data sources and advanced computing hardware and methods [5–7]. In earlier studies, a series of simplified hydrodynamic and hydrological models are developed and applied for simulating overland flow processes in the urban [8]. However, it

is difficult in these simplified models to obtain accurate estimates of the water depths and velocities of the flood waves in urban areas. In fact, floods tend to have rapid velocity and strong destructive power, so accurate simulations of the water depth and flow velocity of floods in low-lying areas near the river are needed. Therefore, many two-dimensional (2D) models based on the solution to the 2D shallow water equations (SWEs) have become popular due to their computational accuracy and efficiency in flood simulations [1, 9, 10]. Particularly, the Godunov-type SWEs models have exhibited great potential for modeling transient overland flows and flash floods due to their shock-capturing capability [11]. Some researchers carried out a series of discussions of a hydraulic analysis of the impact of land use on the run-off regime in a retention area and consequently on flood wave propagation [12, 13]. The impact of land cover on the propagation of flood waves is important to consider the time and spatial characteristics of the riparian and floodplain areas [14]. Similar studies are carried out to investigate the impact of land uses on flood wave propagation in riparian areas and floodplains; this study also applied constant values of the roughness coefficient [15–17]. Vegetation in floodplains significantly reduces water velocities and increases the retention capacity due to levee breaches for the flooding scenarios in the studied area [18].

During the disastrous flood events after intense rainstorms and following dike breaches, in addition to flood mechanical damages, there is also high contamination of floodwater and suspended sediments with inorganic and organic compounds. These pollutants are particularly harmful to public health and the environment and result in deterioration of the water quality [19]. For example, the sewage treatment plants or the treatment ponds that contain pollutants are destroyed by a torrential flood; the released pollutants will rapidly migrate and spread with the floodwater, resulting in significant environmental pollution and damage to densely populated areas. To the best of our current knowledge, an increasing number of numerical studies have been considered to facilitate flood risk management associated with polluted floodwater in urban areas and then to predict the fate of point-source pollutants transported by flood waves in small-scale regions [1, 11, 20, 21]. The mixing and dispersion processes of wastewater surcharging from urban drainage systems within an overland flow are analyzed systematically based on a 2D flood model [22]. A solute transport model based on the Lagrangian particle method is presented to predict the potential contamination paths of pollutants from drainage water in urban areas during a pluvial flood event [23]. Furthermore, a coupled 1D/2D model for hydrodynamic and pollutant transport is developed to carry out the sewer overflow simulation; the results indicate that the model is suitable for simulating the inundation and pollutant transport processes in urban areas [24]. A transport model based on the Lagrangian particle method is proposed to study the potential contamination paths of solutes in drainage water in an urban area during a pluvial flood event [25]. The impact of land uses on nitrogen transport is also investigated to explore how nitrogen transport responds to land-use change and its effects on aquatic habitats in the catchments [26]. A new integrated modeling framework was developed by coupling the Storm Water Management Model (SWMM) to the Cellular-Automata Fast Flood Evaluation model to predict the inundation depth and pollutant transport caused by surcharges over the capacity of the drainage network [27]. In view of the above summary, the land-use change is an important factor for impacting the flood propagation in residential areas, how it interacts, and to what degree it affects flood inundation and pollutant transport that are poorly understood. Under this condition, detailed studies should be conducted to assess the impact of the land-use change on flood inundation and pollutant dispersal in large-scale rural areas.

In this paper, we propose a coupled 2D model to simulate flood disasters and the associated pollutant transport in flood-prone areas. The study is organized as follows: in Section 2, the formulations of the governing equations and a description of the numerical model are presented. In Section 3, the integrated model is validated using several case studies, and the simulated results are compared with the analytical solutions and the measurement data to verify the computation accuracy of the coupling model. Moreover, the study tends to discuss the impact of changed land covers on flood propagation and the pollutant mixing and transport in the areas of Hun and Taizi Lane, China. Lastly, the main conclusions are drawn.

2. Material and Methods

The modeling framework used in this study entails two-dimensional shallow water equations coupled with pollutant mass conservation. The finite volume method with unstructured triangular cells is used to discretize the shallow water equations and pollutant transport equations. The Roe approximate Riemann solution is used to compute the water momentum flux on the interfaces of the triangular mesh. A high-resolution scheme for pollutant transport and diffusion is adopted to deal with the advection term, and a flux limiter is used to reduce artificial diffusion and oscillation. Furthermore, a second-order scheme is adopted to discretize the diffusion term of the solute transport equation.

2.1. Governing Equations. Under the assumption of hydrostatic pressure, the vertical velocity is negligible; a set of SWEs for depth-averaged 2D overland flows over a horizontal plane are deduced [28–30]. The SWEs, which are coupled to the depth-averaged solute transport equation, are written in a compact form:

$$\frac{\partial U}{\partial t} + \frac{\partial F}{\partial x} + \frac{\partial G}{\partial y} = \frac{\partial F_d}{\partial x} + \frac{\partial G_d}{\partial y} + S, \tag{1}$$

where t is the time, U represents the vectors of the conservative variables, F and G are the convection fluxes in the x- and y-directions, respectively, F_d and G_d are the diffusion fluxes in the x- and y-directions, respectively, and S is source term. These parameters are expressed as follows:

$$U = \begin{bmatrix} h \\ hu \\ hv \\ hC \end{bmatrix},$$

$$F = \begin{bmatrix} hu \\ hu^2 + \dfrac{gh^2}{2} \\ huv \\ uhC \end{bmatrix},$$

$$G = \begin{bmatrix} hv \\ huv \\ hv^2 + \dfrac{gh^2}{2} \\ vhC \end{bmatrix},$$

$$F_d = \begin{bmatrix} 0 \\ 0 \\ 0 \\ K_{xx}\dfrac{\partial hC}{\partial x} + K_{xy}\dfrac{\partial hC}{\partial y} \end{bmatrix},$$

$$G_d = \begin{bmatrix} 0 \\ 0 \\ 0 \\ K_{yx}\dfrac{\partial hC}{\partial x} + K_{yy}\dfrac{\partial hC}{\partial y} \end{bmatrix},$$

$$S = \begin{bmatrix} D \\ -\tau_{bx} - ghs_{bx} \\ -\tau_{by} - ghs_{by} \\ S_C \end{bmatrix}, \tag{2}$$

where h is the water depth, u and v are the depth-averaged velocity in the x-direction and y-direction, respectively, g is the gravity acceleration, C is the depth-averaged pollutant concentration, and K_{xx}, K_{xy}, K_{yx}, and K_{yy} are the depth-averaged mixing diffusion coefficients, which can be written as

$$K_{xx} = \frac{\sqrt{g}h\left(\varepsilon_l u^2 + \varepsilon_t v^2\right)}{c\sqrt{u^2 + v^2}},$$

$$K_{xy} = K_{yx} = \frac{\sqrt{g}h\left(\varepsilon_l - \varepsilon_t\right)uv}{c\sqrt{u^2 + v^2}}, \tag{3}$$

$$K_{yy} = \frac{\sqrt{g}h\left(\varepsilon_t u^2 + \varepsilon_l v^2\right)}{c\sqrt{u^2 + v^2}},$$

where c is Chèzy's coefficient; ε_l and ε_t are the dimensionless coefficients of longitudinal dispersion and turbulent diffusion, respectively. In the absence of field measurements, Falconer recommended typical values of $\varepsilon_l = 13.0$ and $\varepsilon_t = 1.2$ [31]. s_{bx} and s_{by} are the bottom slopes in the x-direction and y-direction, $s_{bx} = (\partial Z_b/\partial x)$, $s_{by} = (\partial Z_b/\partial y)$, and Z_b is the bed elevation. S_C indicates the concentration added to the source term per control unit, which is obtained from the wastewater disposal through outfalls. D is the inflow discharge. τ_{bx} and τ_{by} are the bed friction stress values in the x-direction and y-direction; they are defined as

$$\tau_{bx} = g\frac{n^2 u\sqrt{u^2 + v^2}}{h^{1/3}},$$

$$\tau_{by} = g\frac{n^2 v\sqrt{u^2 + v^2}}{h^{1/3}}, \tag{4}$$

where n is Manning's roughness coefficient at the bottom.

2.2. Numerical Discretization. A Godunov-type finite volume method with an unstructured triangular mesh is used for the numerical discretization and solving of the governing equations [32]. The study domain is first divided into a set of control cells, and then an unstructured triangular mesh is created. An explicit time-marching scheme is used in the calculation model. We use the Green formula for integration with the hydrodynamic equation in equation (1); the discrete value of the next time step is obtained from the previous time step as follows:

$$U_i^{n+1} = U_i^n + \frac{\Delta t}{A_i}\left[-\sum_{j=1}^{3}\left(F_{ij} + G_{ij}\right)\cdot n_{ij}\cdot l_{ij} - \sum_{j=1}^{3}\left(F_{d,ij} + G_{d,ij}\right)\cdot n_{ij}\cdot l_{ij} + S_i\right], \tag{5}$$

where U_i^{n+1} and U_i^n are the average values of the control volumes in the current time step and the last time step, respectively, and A_i is the area of the i_{th} mesh element. The solute transport equation (equation (2)) is also integrated using the Green formula; it is expressed as

$$C_i^{n+1} = C_i^n - \frac{\Delta t}{A_i}\sum_{j=1}^{m}\left(Q_{ij}\cdot C_{ij}\right) + \frac{\Delta t}{A_i}\sum_{j=1}^{m}\left(E_{C_{ij}}^{dif}\cdot n_{ij}\right)l_{ij} + \Delta t\cdot S_c, \quad (6)$$

where Q_{ij} represents the flux of the boundary j in the control volume I; $E_{C_{ij}}^{dif}\cdot n_{ij}$ is the pollutant diffusion flux.

The physical variables are the same in every triangular mesh element due to the average depth integration in the equation; a series of piecewise functions are developed in the solution domain. Hence, the unstructured cells exhibit discontinuity at the boundary of each control unit, resulting in a local Riemann problem. The Riemann problem at the cell interface can be solved by using various Riemann approximations for assessing the interface convection fluxes. In this study, the Roe scheme is used to solve the local Riemann problem [21].

The governing equation of the conservative solute transport is the advection-diffusion equation [33]. When convection is dominant in pollutant transport, the problems of numerical oscillation and high artificial diffusion are common in the first-order upwind scheme. The first-order upwind scheme is improved to increase the accuracy by using the flux limit function [34]. Based on the MUST scheme, an r-factor algorithm using the local element to transfer the upwind information is used to reduce the numerical diffusion error due to the upwind approximation of the advection term in this study [35]. A central difference scheme is adopted to discretize the diffusion term in equation (6), which involves the neighboring points in the center of each element. Consequently, the scheme has second-order accuracy and does not require any restrictions regarding the angles of the triangle meshes.

2.3. Variable Time Step. It is common knowledge that the computational stability for an explicit scheme model is limited by the Courant–Friedrichs–Lewy (CFL) condition and the Peclet (Pe) number [36]; therefore, the variable Δt, which is adaptable to the variability of the solute and hydraulic parameters, is dynamically updated. The time step in the explicit scheme must be satisfied with CFL + Pe ≤ 1; these two dimensionless numbers are defined as follows:

$$\mathrm{CFL} = \frac{\max_{i,j}\left(\sqrt{u^2+v^2}+c\right)}{\min\left(d_i\right)}\Delta t_{\mathrm{CFL}}, \quad (7)$$

$$\mathrm{Pe} = \frac{\max_{i,j}\left\{\left|\left(K_{xx}+K_{xy}\right)\cdot n_x + \left(K_{xx}+K_{xy}\right)\cdot n_y\right|\right\}}{\min\left(d_i^2\right)}\Delta t_{Pe}, \quad (8)$$

where d_i is the gird's distance from center to vertices.

3. Simulation Implementation

3.1. Oscillatory Flow in Parabolic Bottom Topography with Friction. In this case study, the oscillation of the free water surface in a parabolic terrain is simulated with bed resistance to verify the ability of the hydrodynamic model for capturing the wet-dry front. The analytical solution of the water level and the bottom topography of the parabolic basin in the oscillatory flow motion are given by [25]. In this experiment, the computational domain is discretized to 18672 triangular grids, the boundary conditions of the study area are fixed wall boundaries, and the initial speed of the study area is 0 m/s. It should be noted that because the boundary of the study area is always in a dry state, the type of boundary condition of the domain does not affect the simulation result. The total simulation time of the water movement is 6000 s, including four and a half cycles. A variable time step is adopted. Figure 1(a) shows the comparison of the numerical and analytical solutions of the water depth at the three gauges (−2750, 0), (−50, 0), and (2750, 0). The measuring points (−2750, 0) and (2750, 0) are located at the junction of the dry and wet areas, and the point (−50, 0) is in a submerged state. The numerical predictions are in perfect agreement with the analytical solutions and no oscillations are detected at the wet-dry interface. The water levels' numerical results of the model and the analytical solution at times 2000 s and 6000 s are shown in Figure 1(b). A strong agreement is observed between the numerical results and analytical solutions of the free surface profile at different times, and the movement of the intersection between the dry and wet areas is accurately captured, with no signs of spurious distortions. The amplitude of the water surface elevation decreases with an increase in the simulation time. At $t = 6000$ s, the water level has stabilized at 10 m, the flow is stable, and the wet-dry intersection point is located at $x = \pm 3000$ m. The results demonstrate that the proposed method is able to determine the moving boundary of the wet and dry areas.

3.2. Solute Transport Simulation. We validate the performance of the proposed model for solving the advection and diffusion equation of solutes in a constant-speed flow field. A pollutant is released at the source, and the migration of the pollutant is calculated. The test is carried out in a 200 m × 800 m rectangular domain, with the north and south boundaries as wall boundaries, the west boundary as the inflow boundary, and the east boundary as the outflow boundary so that free flow is achieved [1]. The entire domain has a flatbed, and the influence of bottom friction is not considered. The initial conditions are $h = 1.0$ m, $u = 1.0$ m/s, and $v = 0.0$ m/s. The analytical value of the initial pollutant concentration field is given as follows:

$$C(t,x,y) = \frac{C_0/h}{4\pi t\sqrt{D_{xx}D_{yy}}}\exp\left(-\frac{(x-x_0-ut)^2}{4K_{xx}t} - \frac{(y-y_0)^2}{4K_{yy}t}\right), \quad (9)$$

where $C_0 = 233.06$ kg, and $x_0 = 0$, $y_0 = 100$, and (x_0, y_0) is where the pollutants are dropped. The mixing coefficients in the x-direction and the y-direction are $K_{xx} = 1.02$ m^2/s and $K_{yy} = 0.094$ m^2/s, respectively. In this case, we set the analytical solution concentration at $t = 60$ s as the initial concentration. In this case study, the computation domain is discretized into 34646 unstructured triangular elements. The simulation time is 600 s, and the time step is variable.

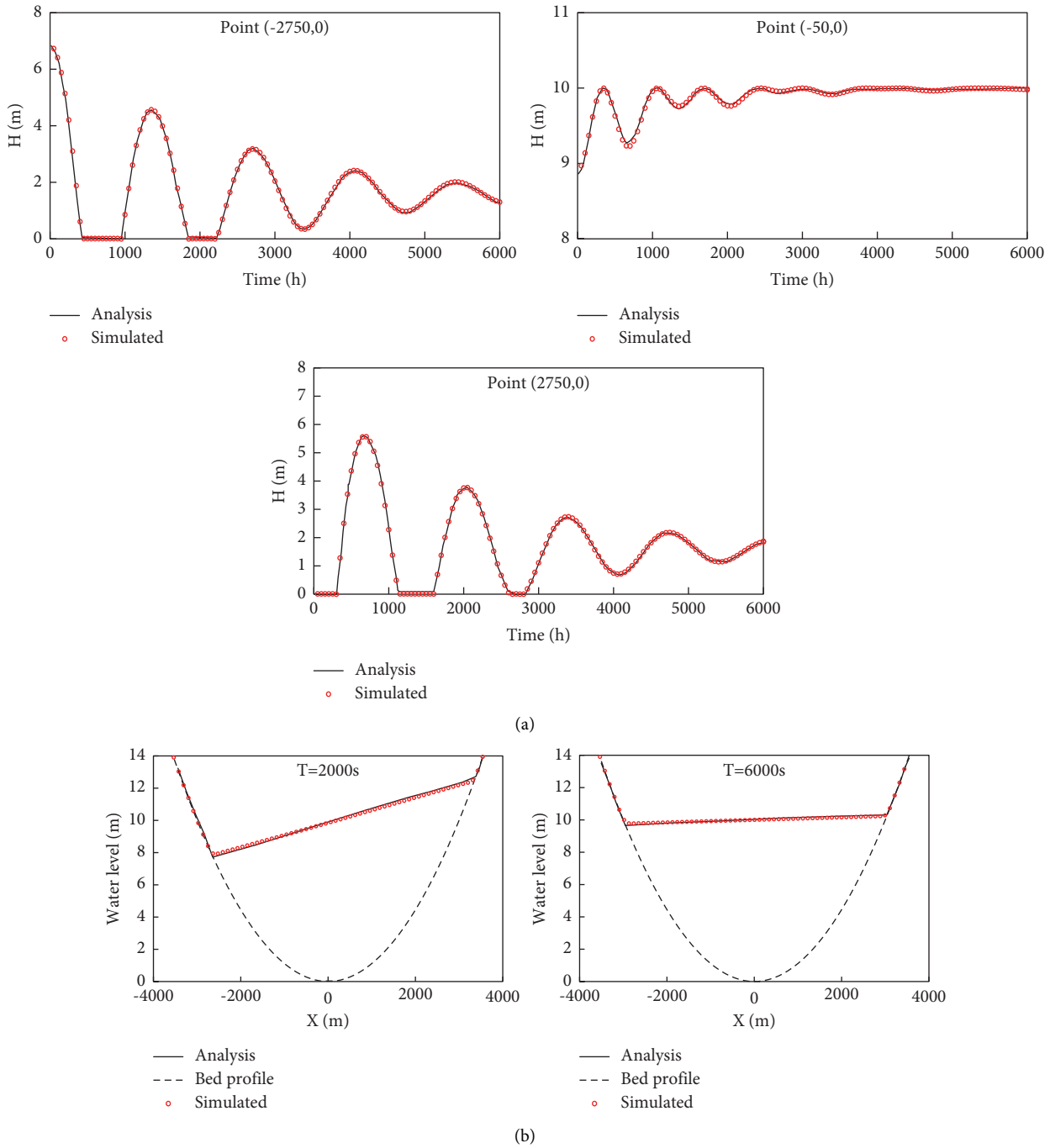

FIGURE 1: Comparison of the numerical results and the theoretical solution in the presence of bed friction. (a) The water depths at different gauges. (b) The water levels at different times.

Figure 2 depicts the solute concentration profiles over time at $y = 100$ m. As the pollutant is transported, the concentration decreases from 1 at the initial state to 0.10 at 600 s. The predicted results are in good agreement with the analytical solutions. The temporal and spatial variations of the predicted pollutant concentration are shown in Figure 3. Under the action of the steady velocity in the x-direction, the pollution mass expands rapidly in the flow direction as it is transported downstream. The diffusion coefficient is larger in the x-direction than in the y-direction, and it is observed that the transverse diffusion amplitude is much higher than that in the longitudinal direction. In summary, the results confirm that the solute transport model accurately simulates the diffusion and movement of contaminants in water.

3.3. Simulation Flood Propagation in the HTL. The Liao River basin is one of the largest hydrological systems in China; its watershed area is about 21.9×10^4 km^2, and the main river is the Liao River. The Hun River and the Taizi River are two

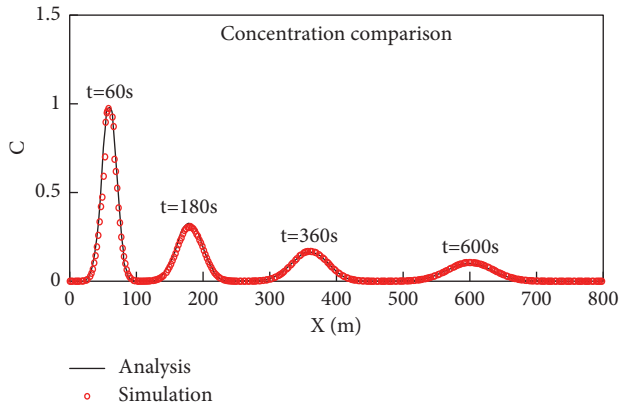

Figure 2: Comparison of the simulated and analytical concentrations at different times in the x-direction.

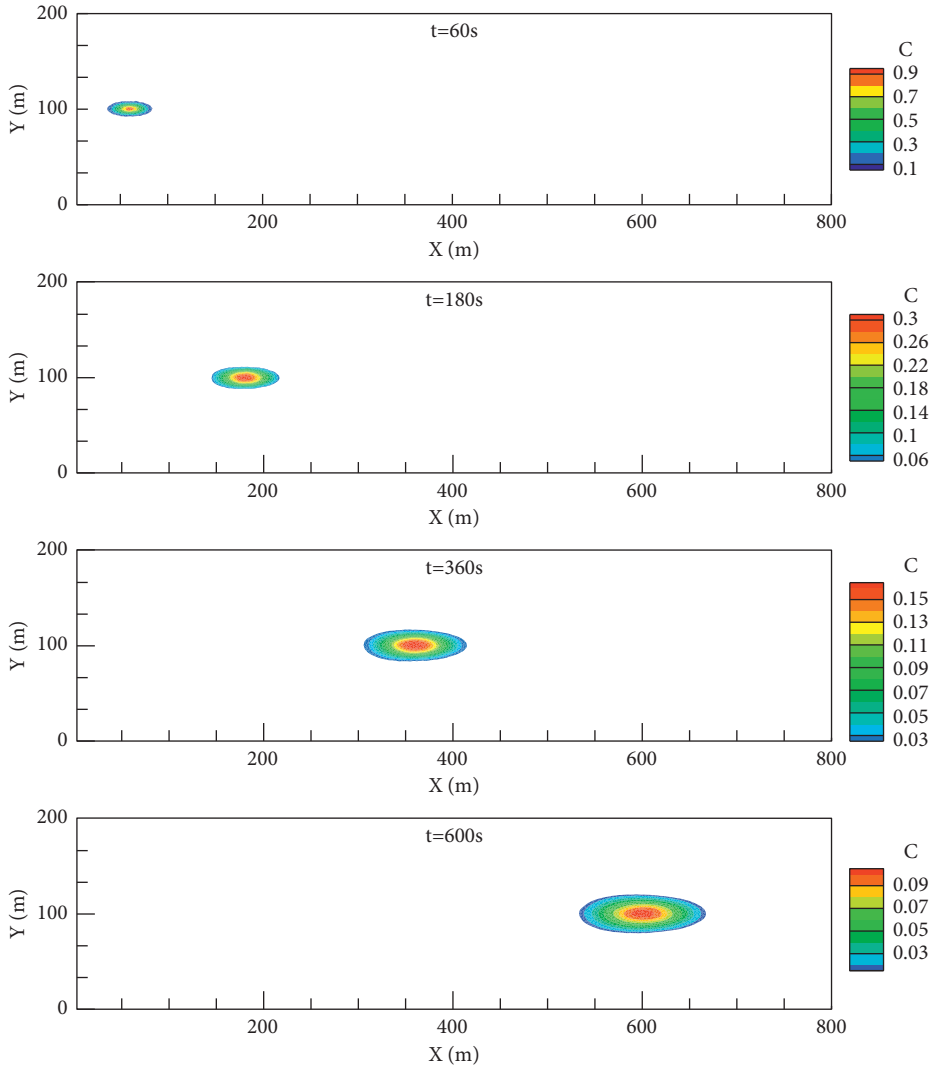

Figure 3: Advection and diffusion of a solute cloud: concentration field at different times.

main tributaries of the Liao River, and the two rivers flow southwest in parallel. After the confluence of the Sanchahe in Haicheng City, the river is called the Da Liao River. The Da Liao River empties into the Liao River estuary at Yingkou City and eventually flows into the Bohai Sea. In the section of the Hun River and the Taizi River, the left embankment of the Hun River and the right embankment of the Taizi River form an alley, which is referred to as the HTL (Figure 4). The HTL includes the Xiaobeihe area in Liaoyang County, the Gaotuozi area in Haicheng, the Tangmazhai area, and

Figure 4: The location of the HTL.

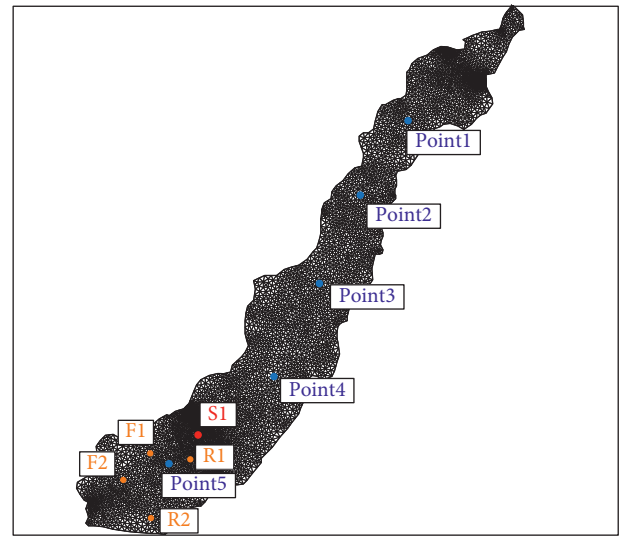

Figure 5: The unstructured triangular mesh in the HTL area.

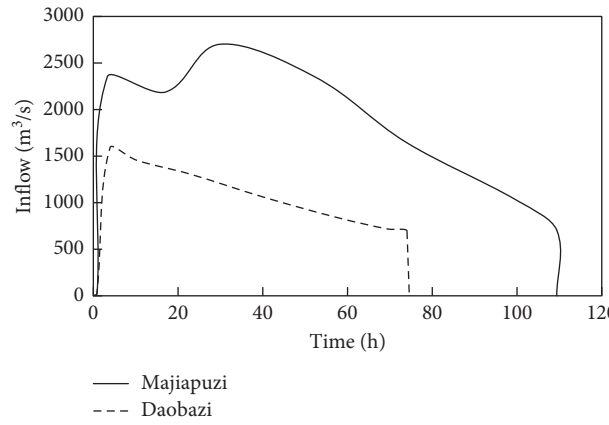

Figure 6: Discharge hydrographs at the dike break sites.

Wenxiang city. Where the terrain of the HTL is high in the north and low in the south, the maximum difference of terrain elevation is about 11 meters in the whole study domain. The overall terrain is flat and the fluctuations are less dramatic.

Heavy rainfall has a significant impact on the water levels of the Hun River and Taizi River during the flood season. According to historical statistics, flood and waterlogging disasters frequently occurred in the Hun River and Taizi River. A total of 114 floods of varying degrees have occurred in the nearly two hundred years from 1798 to 1997; among them, there are 20 large-scale flood disasters. For example, the city of Majiapuzi near the Taizi River has seen many levee breaches with the heavy flood inundation in 1949 and 1950, and in Daobazi close to the Hun River, a levee break occurred during the great flood of 1995. Large floods have caused significant damage to the urban and rural areas in the HTL. In this study, we use the HTL as a case study and simulate the processes of dike break flood caused by heavy rainfall with a 100 year return period. Daobazi and Majiapuzi are chosen as the dike break sites to simulate a major flood in the HTL; the locations of Daobazi and Majiapuzi are shown in Figure 5. Figure 6 presents the discharge hydrographs of the two dike breach sites. The initial state of the study area is a dry bed, the total duration of the simulation is 120 h, and the initial Manning coefficient is $n = 0.025\ \mathrm{s/m}^{1/3}$ in the entire domain. A variable time step is adopted in the simulation to reduce the running time. In shallow water models, an increase in the cell sizes improves the simulation accuracy, but the computational cost increases accordingly. Firstly, we study the flood motion of the dike breach in Majiapuzi station at three different mesh resolutions to determine the most appropriate grid accuracy; five gauges are selected to analyze the processes of flood waves and their location is shown in Figure 5. As shown in Figure 7, the time series of water depth (Figure 7(a)) and the maximum depth (Figure 7(b)) at different gauges corresponding to three mesh resolutions are compared, and the time series of the maximum submerged area (Figure 7(c)) under three resolution grids are also revealed. We can see that the simulated values of water depth and the maximum water depth at the selected gauges almost have no difference under the condition of three grid resolutions, and the submerged area at several gauges is also basically consistent. So we select the mesh accuracy with a total of 9585 unstructured triangular elements, which can complete the calculation at the minimum computational cost and maintain sufficient accuracy. The length of the grid edge around the inflow boundary is small (30~50 m); the spatial grid size is large in the regions outside of the dike break site

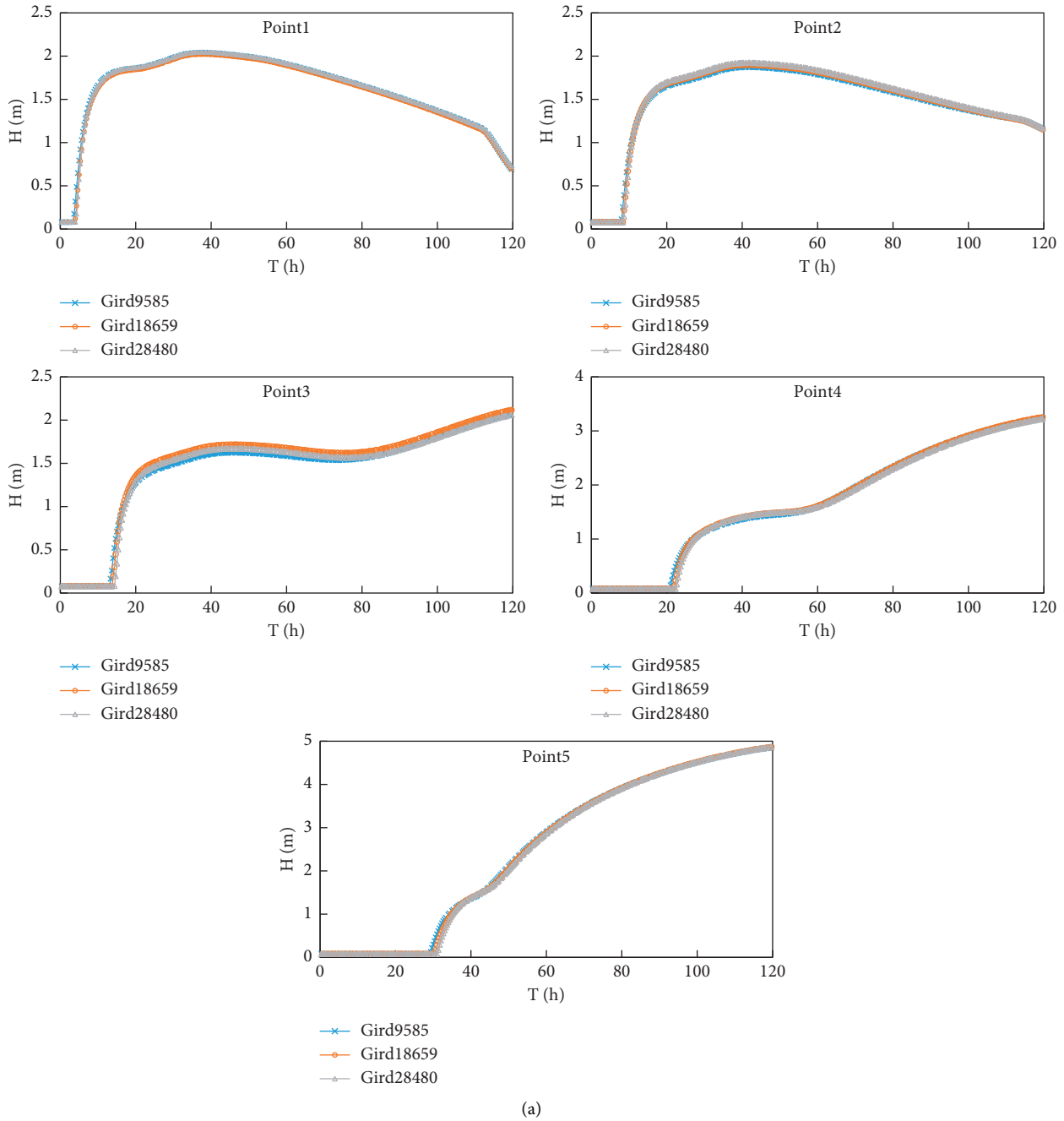

(a)

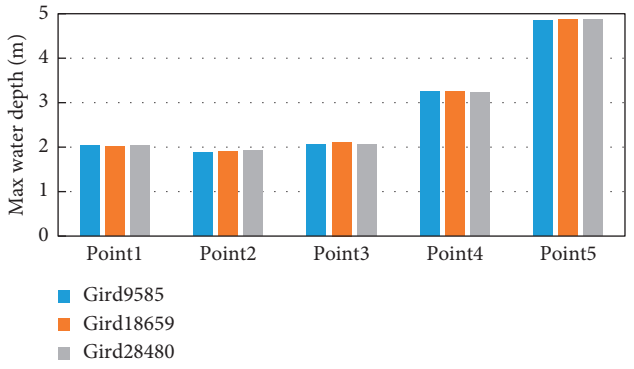

(b)

Figure 7: Continued.

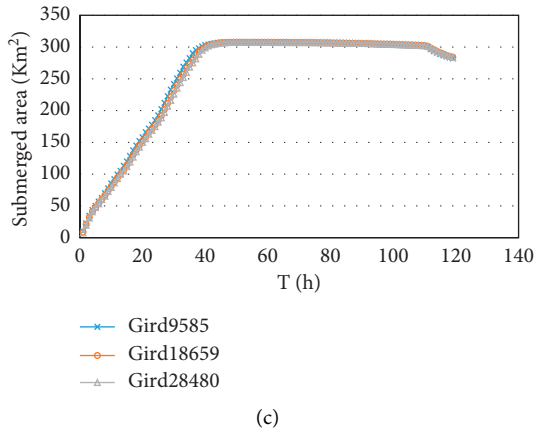

(c)

Figure 7: Comparison of the simulated variables at different grid resolutions. (a) The time series of water depth at different gauges. (b) Max water depth at different gauges. (c) The time series of submerged area.

to reduce the calculation time. Comparisons of the submerged area are made between the proposed model and the HEC, CUIDES, and FEM models as shown in Figure 8, the results show relatively few differences in the submerged area between these models, and the simulated results from the present model show good computational accuracy. Figure 9(a) shows the inundation range and flow field distribution of the Majiapuzi flood at different times. The floodwater moves from the northeast to the southwest, which is consistent with the terrain of the "Huntai lane" that is higher in the northeast and lower in the southwest. After the dike breach, the submerged area continues to expand, and the floodwater is accumulating downstream. Figure 9(b) shows the flood inundation range and flow field distribution of the Daobazi dike breach at different times. The floodwater moves from the northeast to the southwest. The flood velocity decreases significantly after the inflow discharge has weakened and the flow has stabilized.

4. Results and Discussion

4.1. Flood Simulation Scenarios for Changed Land Uses. In the simulation of overland flow caused by a dike breach of the river, important field parameters which affect the model performance are Manning's roughness coefficient values in different catchments. HTL is one of the important residential areas and the grain-producing areas in north China, the roles of farmland vegetation and residence area have a crucial impact on the flooding wave processes. It is known to all that remote sensing (RS) data, acquired by optical and microwave sensors mounted on satellites and airplanes, are important alternative sources of information for mapping land use/cover. The objective of the present research is to adopt RS technology to obtain the distribution of residence area and farmland vegetation in the domain of the HTL. The RS images of the HTL area are acquired from Landsat8 Operational Land Imager (OLI), provided by the USGS (https://glovis.usgs.gov/next/). In this computation domain, the emphasis of information extraction is building, waterbody, and farmland vegetation. The normalized difference vegetation index and modified normalized difference water index are used to extract objects. The decision tree classification is used to realize the extraction of buildings and houses, farmland areas, and waterbodies (Figure 10). Land use/cover classes observed in this figure are vegetation land (82.21%), built-up areas (6.71%), and waterbodies (0.92%) in HTL. The value of Manning's coefficient on the basis of available data on the distribution of land use is set to be 0.13 and 0.05 in the residential district and farmland area, respectively [37, 38]. We select four stations in farmland (F1, F2) and residential areas (R1, R2) to simulate the variation of water depth and flow velocity. As can be seen from Figures 11(a) and 11(b), owing to the rapid flow rate of a flood near the dike break position, the amount of water is temporarily accumulated in a short time at F1 and R1 under the action of farmland and architecture resistance, which increased the water depth at these two stations. The flood arrival time of F2 and R2 gauges is delayed by 2.5 h and 5 h, respectively. Figure 11(c) shows the simulated velocity of flood waves under the condition of different Manning coefficients; the results indicate that the increase of bed resistance attenuates the peak velocity of flood waves and its amplitude decreases by about 40%; the arrival time of the peak velocity is delayed as well. As shown by these values, the presence of the vegetation induced a significant decrease in velocity values. In the later stage of flood evolution, with the increase of floodwater volume, the water depths at the gauges keep constant, where it reaches the state of hydrostatic equilibrium. Generally speaking, the changes of land use in the presence of the residential building, vegetation, and farmland crop not only significantly reduce the effects of the flood wave in the study area but also cause the mitigation of the flood wave and so its effect decreases through the downstream part of the studied area.

We assume that during the evolution of the flood in the Daobazi dike breach, a sewage treatment plant is destroyed by the floodwater in Zhujiajie Village, Wenxiang Town; this allows us to model the transport process of pollutants in a flood of HTL. The solute release point is placed at S1 as shown in Figure 5. The contaminant transports start at the 10th hour after dike break, while the concentration is $C = 20$ mg/L and the release of pollutants lasts for 10 hours in

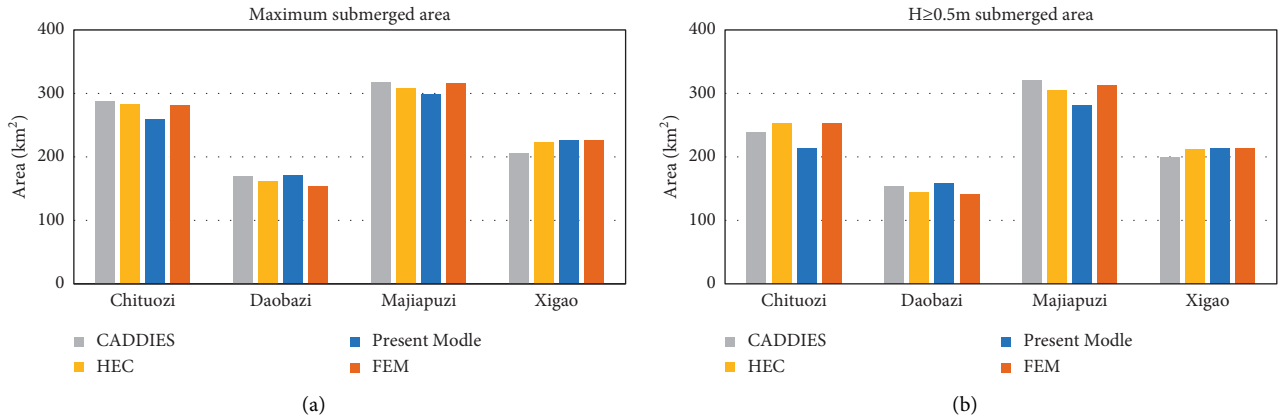

Figure 8: Comparison of the submerged areas in four scenarios for the different flood models.

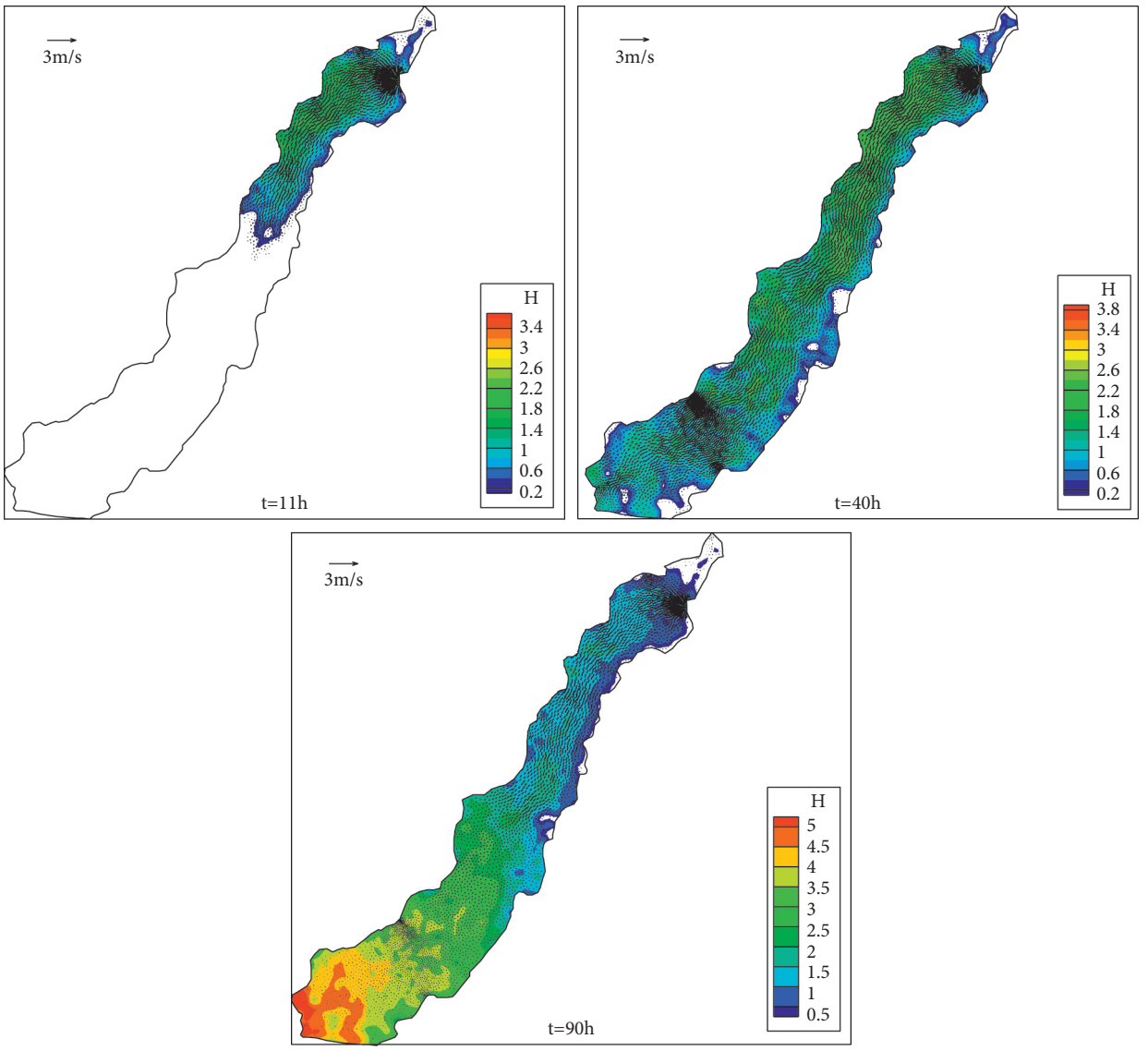

Figure 9: Continued.

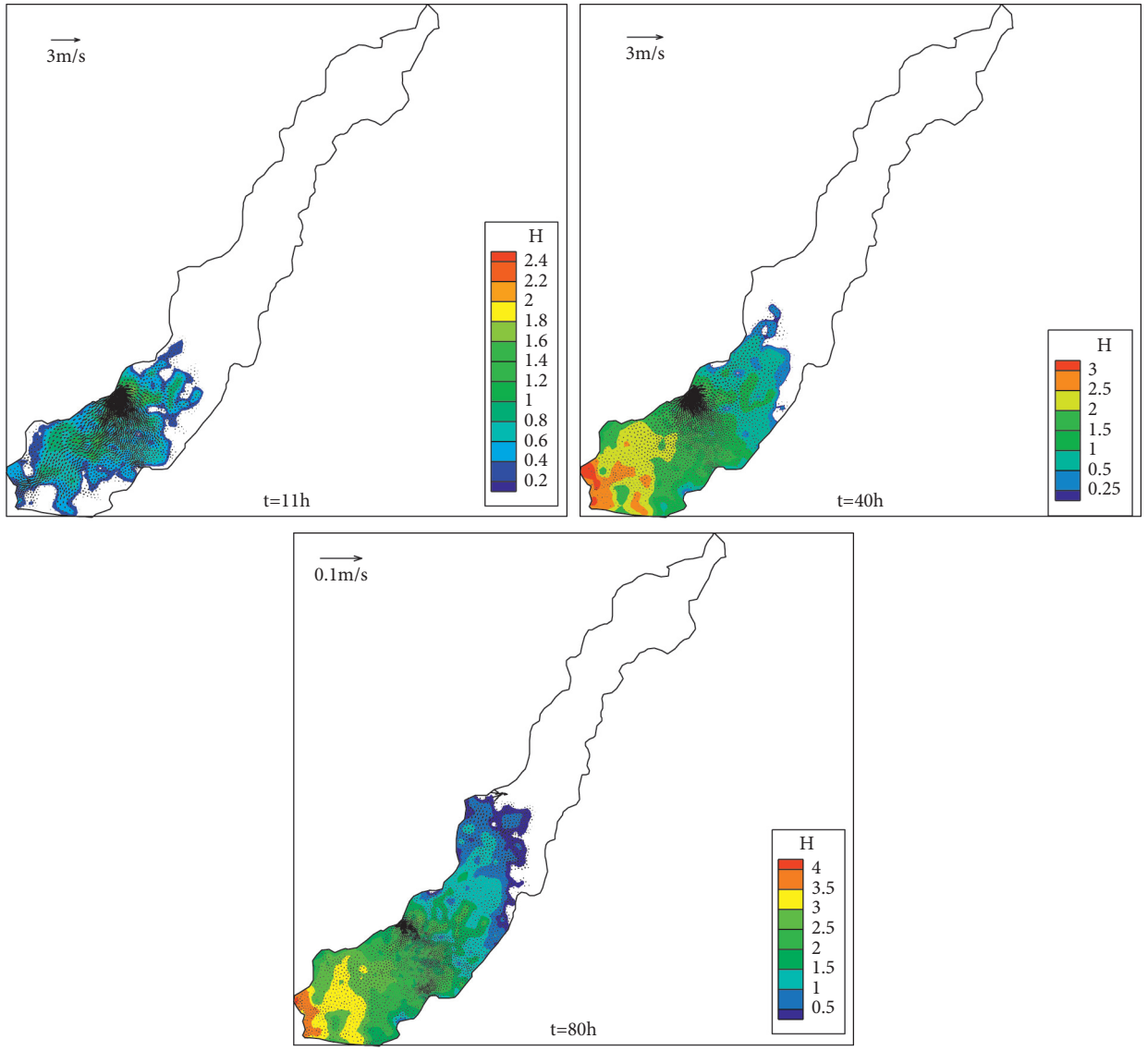

(b)

Figure 9: The movement of the floodwater at different times. (a) Majiapuzi dike breach and (b) Daobazi dike breach.

this case study. In the simulation of the Daobazi dike breach, Figure 12 shows the pollutant transport associated with the overland flow at different times without and with considering the land use types. It is obvious from comparing Figure 12 that the pollutant plume appears a narrower shape using a single Manning's roughness value in the computation domain compared to that in the situation of considering different land uses, these are all attribute to the variation of overland flow velocity caused by the resistance of farmland and building. After 20 hours at the end of the release, we observe that the highest concentration of the pollutants moves along the movement direction of the flood waves in both cases. The role of advection transport is extremely important compared to diffusion transport during the pollutant process evolution in the flood events; therefore, if the flood waves move fast, the pollutants will quickly spread downstream with the flood waves.

Simulation experiments are also conducted with the pollutant transport subjected to isotropic and anisotropic diffusion driven by the river dike breach flood waves. We set the mixing coefficients ε_l and ε_t in equation (3) to 13 and 1.2 for anisotropic diffusion, respectively. For isotropic dispersion, the mixing coefficients are both set to 13. In simulating the pollutant transport following the flood, the effect of farmland and residence resistance is considered; the evolution of the pollutant plume at different times for the anisotropic is compared with the isotropic case in Figure 13. Because of the isotropic dispersion, the pollutant in floodwater spreads faster in a transverse direction than that due to anisotropic diffusion. It is worth mentioning that the locations of the peak pollutant concentration are mainly controlled by the advection. With the increase in transport time, the region of low pollutant concentration will be larger than that

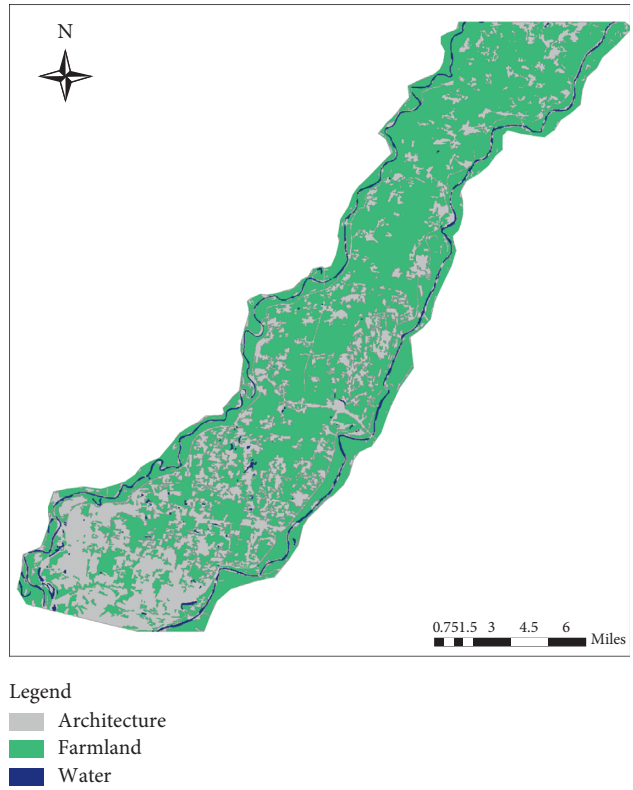

Figure 10: Land use/cover map using satellite imagery.

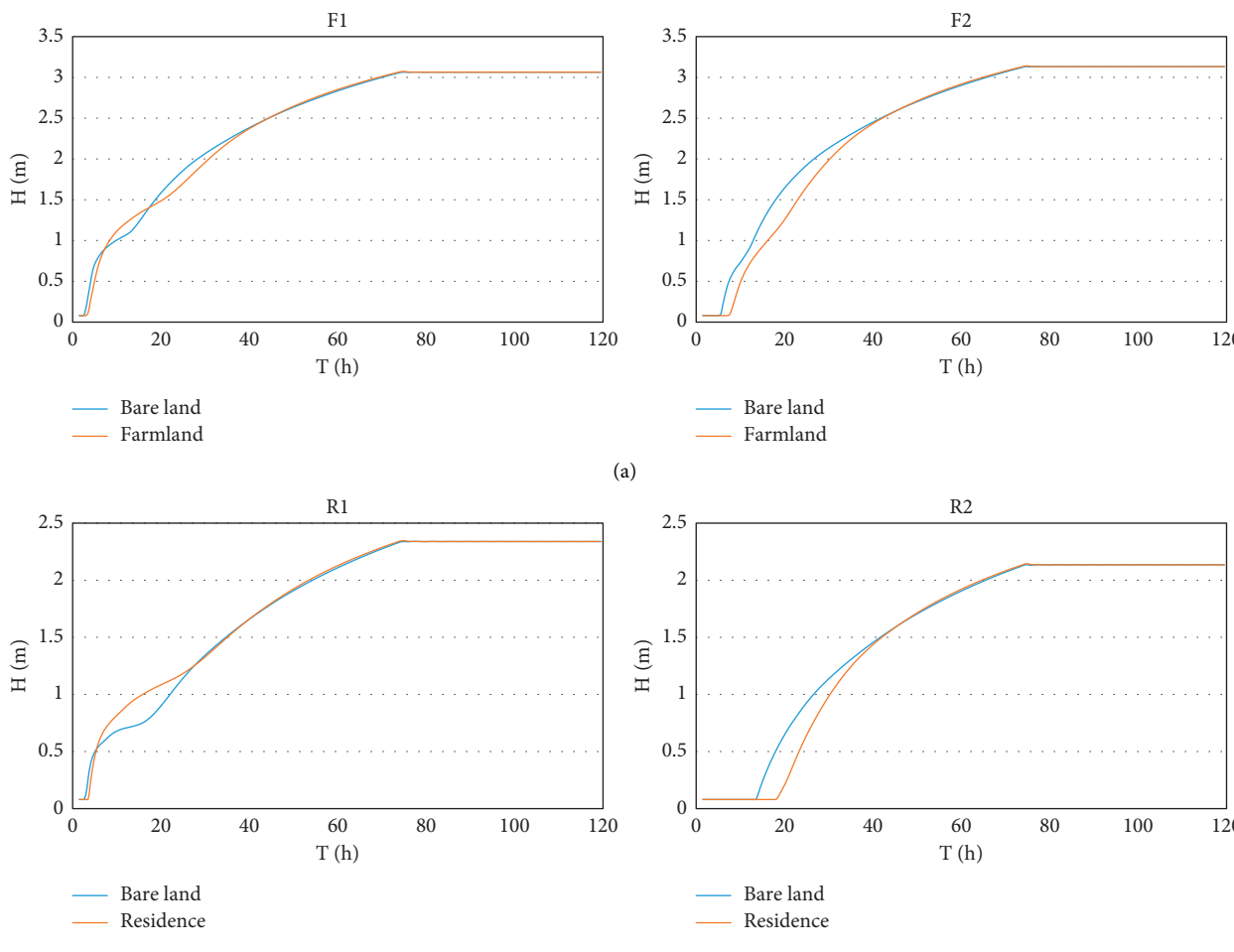

Figure 11: Continued.

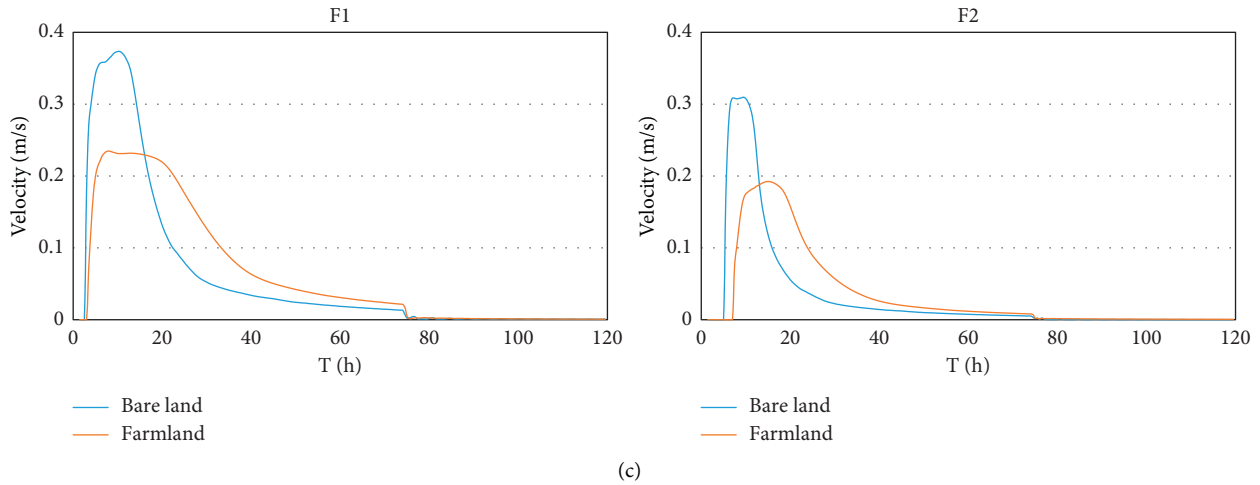

(c)

Figure 11: Comparison of the simulated water depths and velocities with varied land uses. Simulation of flood-related water pollution in the HTL. (a) Comparison of the flow depth between bare land and farmland. (b) Comparison of the flow depth between bare land and residence. (c) Comparison of the flow velocity between bare land and farmland.

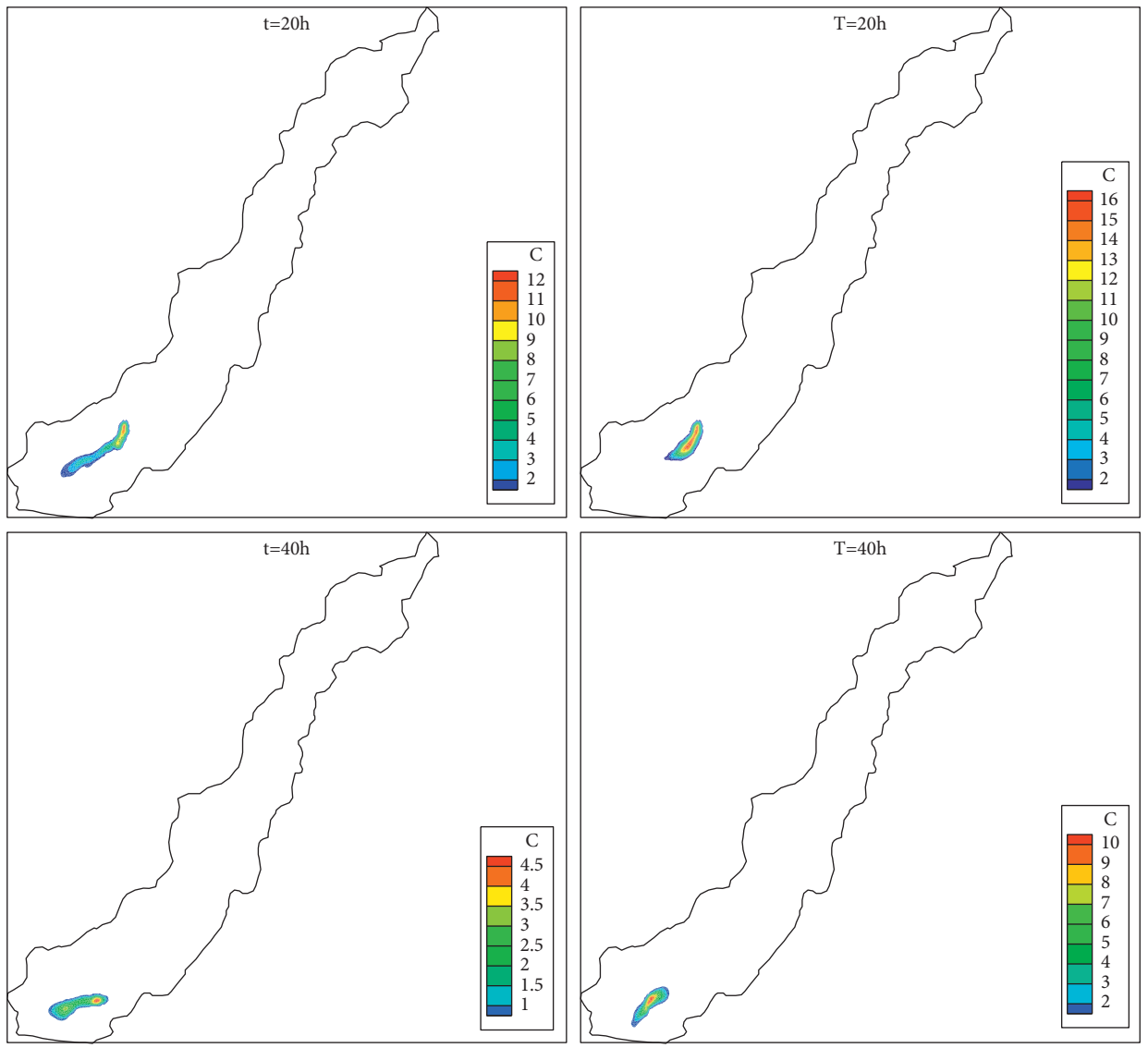

Figure 12: The transport of the pollutants without (left) and with (right) considering land-use type.

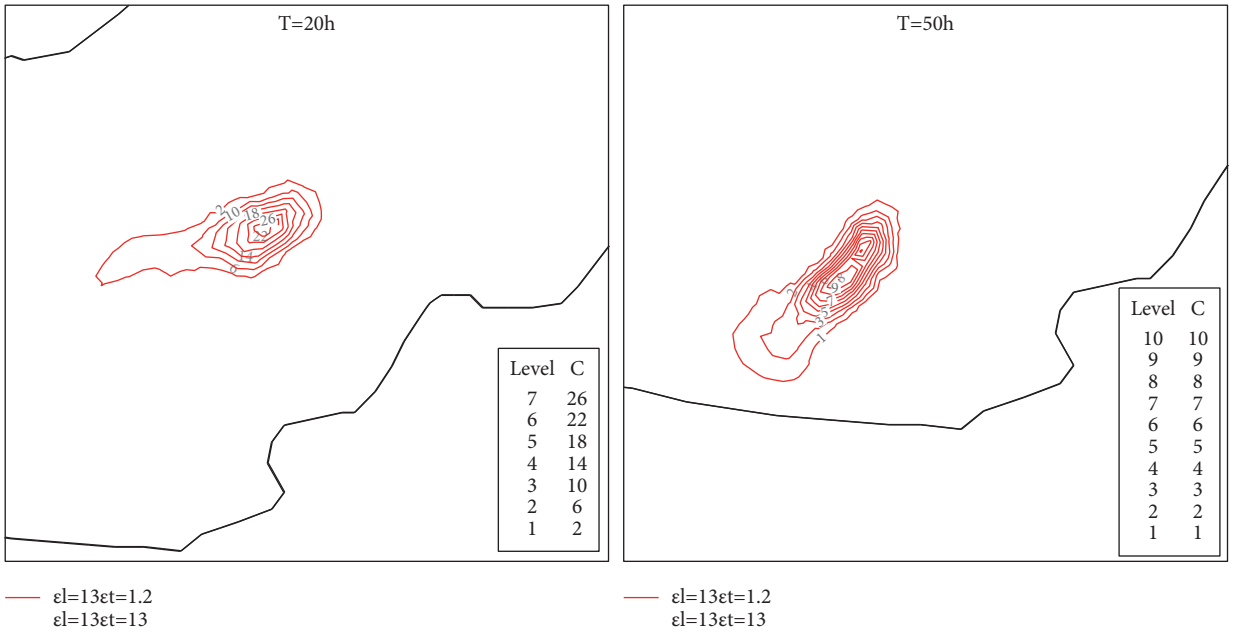

Figure 13: Comparison of the isotropic and anisotropic diffusion of pollutants with considering land-use types.

under the action of anisotropy diffusion; the concentrations in pollutant centers are significantly low due to the effect of isotropic dispersion. This is caused by the excessive spreading of the pollutant in the transverse direction under isotropic diffusion. The overall development of the pollutant concentration movement and distribution for the anisotropic diffusion is found to be rational.

5. Conclusions

In the present paper, a fully coupled model on solute transport following a flood is proposed to simulate the flow hydrodynamics and the process of pollutant transport in flood-prone districts. Subsequently, the involved model is successfully validated using several tests with satisfactory results, confirming its numerical stability and computational accuracy with shock capture capacity. Moreover, this study shows that the model performs well for a prolonged flood in the HTL area with complex 2D topography during a short time in a large-scale domain. Considering the potential influence of the land-use change on flood events, we focus mainly on the response of flood wave propagation and associated pollutant transport to land cover patterns changes in residential areas. In this simulation, we consider a spatial variation of the roughness using a mesh in which each node has a roughness coefficient depending on the type of land uses; the flood hydraulics are also compared. The results indicate that water depth and flow velocity are sensitive to the variation of the different land-use types; the propagation process of flood waves slows down after considering the resistance of farmland and residential areas, so any considerable change in land use significantly influences the behavior of flood risk during flood events in HTL. In particular, this study also indicates that the pollutant transport is more dynamic following flood inundation in the HTL area, and the land cover plays an important role in the mixing and transport of pollutants in the rapidly varying flood events. In addition, the results of anisotropic diffusion are more reasonable than those of isotropic dispersion in simulating pollutant transport in a real flood study. In general, the present model can quickly predict flood inundation and flood-related water pollution for real-world flood simulations.

In fact, HTL areas have distinct types of plants: grassland, shrubs, forests, or crop. Flood inundation changes from partial submergence to complete submergence for different plants, the resistances caused by plants for different land covers vary with the water depth. One can see that the drag force caused by plants is able to totally describe the flow and resistance in vegetated areas; therefore, this method should be understood and quantified in future work.

Data Availability

All data included in this study are available upon request by contact with the corresponding author.

Conflicts of Interest

The authors declare that they have no conflicts of interest.

Acknowledgments

This work was supported by the National Nature Science Foundation of China (51879028), the National Key R&D Program of China (2019YFC1407704), and the Open Fund of State Key Laboratory of Coastal and Offshore Engineering, Dalian University of Technology (LP2009).

References

[1] L. Zhang, Q. Liang, Y. Wang, and J. Yin, "A robust coupled model for solute transport driven by severe flow conditions," *Journal of Hydro-environment Research*, vol. 9, no. 1, pp. 49–60, 2015.

[2] B. Jongman, S. Hochrainer-Stigler, L. Feyen et al., "Increasing stress on disaster-risk finance due to large floods," *Nature Climate Change*, vol. 4, no. 4, pp. 264–268, 2014.

[3] T. J. Fewtrell, P. D. Bates, M. Horritt, and N. M. Hunter, "Evaluating the effect of scale in flood inundation modelling in urban environments," *Hydrological Processes*, vol. 22, no. 26, pp. 5107–5118, 2008.

[4] B. Merz, H. Kreibich, R. Schwarze, and A. Thieken, "Review article "Assessment of economic flood damage"," *Natural Hazards and Earth System Sciences*, vol. 10, no. 8, pp. 1697–1724, 2010.

[5] Y. Fan, T. Ao, H. Yu, G. Huang, and X. Li, "A coupled 1D-2D hydrodynamic model for urban flood inundation," *Advances in Meteorology*, vol. 2017, Article ID 2819308, 12 pages, 2017.

[6] H. K. McMillan and J. Brasington, "Reduced complexity strategies for modelling urban floodplain inundation," *Geomorphology*, vol. 90, no. 3-4, pp. 226–243, 2007.

[7] T. J. Coulthard, J. C. Neal, P. D. Bates, J. Ramirez, G. A. M. de Almeida, and G. R. Hancock, "Integrating the LISFLOOD-FP 2D hydrodynamic model with the CAESAR model: implications for modelling landscape evolution," *Earth Surface Processes and Landforms*, vol. 38, no. 15, pp. 1897–1906, 2013.

[8] R. S. Govindaraju, S. E. Jones, and M. L. Kavvas, "On the diffusion wave model for overland flow: 1. Solution for steep slopes," *Water Resources Research*, vol. 24, no. 5, pp. 734–744, 1988.

[9] J. Xia, R. A. Falconer, B. Lin, and G. Tan, "Numerical assessment of flood hazard risk to people and vehicles in flash floods," *Environmental Modelling & Software*, vol. 26, no. 8, pp. 987–998, 2011.

[10] A. Ferrari, S. Dazzi, R. Vacondio, and P. Mignosa, "Enhancing the resilience to flooding induced by levee breaches in lowland areas: a methodology based on numerical modelling," *Natural Hazards and Earth System Sciences*, vol. 20, no. 1, pp. 59–72, 2020.

[11] J. Murillo, P. García-Navarro, J. Burguete, and P. Brufau, "A conservative 2D model of inundation flow with solute transport over dry bed," *International Journal for Numerical Methods in Fluids*, vol. 52, no. 10, pp. 1059–1092, 2006.

[12] G. Rak, D. Kozelj, and F. Steinman, "The impact of floodplain land use on flood wave propagation," *Natural Hazards*, vol. 83, no. 1, pp. 425–443, 2016.

[13] I. Haltas, S. Elçi, and G. Tayfur, "Numerical simulation of flood wave propagation in two-dimensions in densely populated urban areas due to dam break," *Water Resources Management*, vol. 30, no. 15, pp. 5699–5721, 2016.

[14] M. Rogger, M. Agnoletti, A. Alaoui et al., "Land use change impacts on floods at the catchment scale: challenges and opportunities for future research," *Water Resources Research*, vol. 53, no. 7, pp. 5209–5219, 2017.

[15] B. Andersen, I. Rutherfurd, and A. Western, "An analysis of the influence of riparian vegetation on the propagation of flood waves," *Environmental Modelling & Software*, vol. 21, no. 9, pp. 1290–1296, 2006.

[16] A.-R. Ghavasieh, C. Poulard, and A. Paquier, "Effect of roughened strips on flood propagation: assessment on representative virtual cases and validation," *Journal of Hydrology*, vol. 318, no. 1–4, pp. 121–137, 2006.

[17] J. E. Schubert, B. F. Sanders, M. J. Smith, and N. G. Wright, "Unstructured mesh generation and landcover-based resistance for hydrodynamic modeling of urban flooding," *Advances in Water Resources*, vol. 31, no. 12, pp. 1603–1621, 2008.

[18] H. Thomas and T. R. Nisbet, "An assessment of the impact of floodplain woodland on flood flows," *Water and Environment Journal*, vol. 21, no. 2, pp. 114–126, 2007.

[19] N. H. Tran, M. Reinhard, E. Khan et al., "Emerging contaminants in wastewater, stormwater runoff, and surface water: application as chemical markers for diffuse sources," *The Science of the Total Environment*, vol. 676, pp. 252–267, 2019.

[20] F. Behzadi, B. Shamsaei, and J. C. Newman III, "Solution of fully-coupled shallow water equations and contaminant transport using a primitive-variable Riemann method," *Environmental Fluid Mechanics*, vol. 18, no. 2, pp. 515–535, 2018.

[21] M. Morales-Hernández, J. Murillo, and P. García-Navarro, "Diffusion-dispersion numerical discretization for solute transport in 2D transient shallow flows," *Environmental Fluid Mechanics*, vol. 19, pp. 1217–1234, 2019.

[22] O. Mark, C. Jørgensen, M. Hammond et al., *A New Methodology for Modelling of Health Risk from Urban Flooding Exemplified by Cholera—Case Dhaka, Bangladesh*, pp. 28–42, Blackwell Publishing Inc., Hoboken, NJ, USA, 2018.

[23] J. Sampson, A. Easton, and M. Singh, "Moving boundary shallow water flow above parabolic bottom topography," *ANZIAM Journal*, vol. 47, pp. C373–C387, 2005.

[24] A. Pathirana, M. D. Maheng, and D. Brdjanovic, "A Two-dimensional pollutant transport model for sewer overflow impact simulation," in *Proceedings of the 12nd International Conference on Urban Drainage*, pp. 10–15, Porto Alegre, Brazil, September 2011.

[25] R. Sämann, T. Graf, and I. Neuweiler, "Modeling of contaminant transport during an urban pluvial flood event—the importance of surface flow," *Journal of Hydrology*, vol. 568, pp. 301–310, 2019.

[26] X. Chen, Y. Wang, Z. Cai, C. Wu, and C. Ye, "Effects of land-use and land-cover change on nitrogen transport in northern taihu basin, China during 1990–2017," *Sustainability*, vol. 12, no. 9, p. 3895, 2020.

[27] B. Jamali, P. M. Bach, and A. Deletic, "Rainwater harvesting for urban flood management—an integrated modelling framework," *Water Research*, vol. 171, 2020.

[28] J. Tang, D. Causon, C. Mingham, and L. Qian, "Numerical study of vegetation damping effects on solitary wave run-up using the nonlinear shallow water equations," *Coastal Engineering*, vol. 75, pp. 21–28, 2013.

[29] C. Di Cristo, M. Greco, M. Iervolino, and A. Vacca, "Interaction of a dam-break wave with an obstacle over an erodible floodplain," *Journal of Hydroinformatics*, vol. 22, no. 1, pp. 5–19, 2020.

[30] Z. Horváth, A. Buttinger-Kreuzhuber, A. Konev et al., "Comparison of fast shallow-water schemes on real-world floods," *Journal of Hydraulic Engineering*, vol. 146, no. 1, pp. 1–16, 2020.

[31] R. A. Falconer, "Review of modelling flow and pollutant transport processes in hydraulic basins," in *Water Pollution: Modelling, Measuring and Prediction*, L. C. Wrobel and C. A. Brebbia, Eds., pp. 3–23, Springer, Dordrecht, Netherlands, 2nd edition, 1991.

[32] X. Liu, B. J. Landry, and M. H. García, "Two-dimensional scour simulations based on coupled model of shallow water equations and sediment transport on unstructured meshes," *Coastal Engineering*, vol. 55, no. 10, pp. 800–810, 2008.

[33] F. Yang, D. Liang, X. Wu, and Y. Xiao, "On the application of the depth-averaged random walk method to solute transport simulations," *Journal of Hydroinformatics*, vol. 22, no. 1, pp. 33–45, 2020.

[34] V. Casulli and P. Zanolli, "High resolution methods for multidimensional advection-diffusion problems in free-surface hydrodynamics," *Ocean Modelling*, vol. 10, no. 1-2, pp. 137–151, 2005.

[35] M. Zhang, Y. Xu, and H. Qiao, "Numerical study of hydrodynamic and solute transport with discontinuous flows in coastal water," *Environmental Modeling & Assessment*, vol. 23, no. 4, pp. 353–367, 2018.

[36] X. Liu, "A robust numerical model for shallow water governing solute transport with wet/dry interfaces," *Computer Methods in Applied Mechanics and Engineering*, vol. 351, pp. 85–108, 2019.

[37] K. El Kadi Abderrezzak, A. Paquier, and E. Mignot, "Modelling flash flood propagation in urban areas using a two-dimensional numerical model," *Natural Hazards*, vol. 50, no. 3, pp. 433–460, 2009.

[38] C.-J. Huang, M.-H. Hsu, W.-H. Teng, and Y.-H. Wang, "The impact of building coverage in the metropolitan area on the flow calculation," *Water*, vol. 6, no. 8, pp. 2449–2466, 2014.